STATISTICS, OPTIMIZATION AND INFORMATION COMPUTING
Stat., Optim. Inf. Comput., Vol. **13**, May 2025, pp 2079–2104.
Published online in International Academic Press (www.IAPress.org)

Mathematical Modeling and Numerical Simulation of Central Retinal Artery Occlusion (CRAO) with Asymmetric Stenosis

Arif Fatahillah[1,2], Basuki Widodo[1,*], Rozaini Roslan[3]

[1]*Department of Mathematics, Sepuluh Nopember Institute of Technology, Surabaya, Indonesia*
[2]*Department of Mathematics Education, University of Jember, Jember, Indonesia*
[3]*Department of Mathematics and Statistics, Faculty of Applied Sciences and Technology, Universiti Tun Hussein Onn Malaysia, Pagoh Campus, 84600 Muar, Johor, Malaysia*

Abstract This study focuses on the analysis of arterial blood flow through a stenotic region with asymmetric stenosis in the case of Central Retinal Artery Occlusion (CRAO). Three different stenotic shapes are examined in this research: Bell-Cosine shape, Cosine-Elliptical shape, and Bell-Elliptical shape. The present study marks the first initiative to perform numerical analysis on three stenotic shapes. The finite volume method was employed to construct the blood flow model, which was solved using the SIMPLE algorithm. To support the implementation of this model, several simulation comparisons were made with existing models, and computational results for various parameter values were presented as contours and graphs. Numerical simulations were conducted to investigate the influence of the stenosis shape, position, and thickness on the velocity and pressure in the retinal blood vessels. High flow profiles with minor disturbances are observed near the origin of the stenotic artery for all geometric shapes. The pressure profile also shows elevated values near the sharp edges of the stenotic region. Among the three models, the Cosine-Elliptical shape yields the highest flow velocity, while the Bell-Cosine shape produces the highest pressure and wall shear stress. The validation of MATLAB results using ANSYS confirmed the accuracy of the model, ensuring that the MATLAB simulation is reliable for further studies.

Keywords Blood flow; Bell shape; Cosine shape; Elliptical shape; SIMPLE algorithm

AMS 2010 subject classifications 35R10, 35R12, 35R70, 76M10

DOI: 10.19139/soic-2310-5070-2381

1. Introduction

Central Retinal Artery Occlusion (CRAO) is a medical emergency characterized by the sudden cessation of blood flow in the central retinal artery [1](Figure 1). This condition can lead to significant and often permanent vision loss in the affected eye. According to Hoyer et al. [2] and Grory et al. [3], CRAO is typically caused by embolism or thrombosis, which blocks blood flow to the retina, resulting in rapid tissue damage. Early diagnosis and proper management are essential for reducing retinal damage and maximizing the potential for visual recovery [4, 5]. Clinically, CRAO requires swift and accurate evaluation to determine the cause and severity of the occlusion. Common diagnostic steps include fundoscopic examination, fluorescein angiography, and Optical Coherence Tomography (OCT). These tests help identify the characteristic features of CRAO, such as retinal color changes and the presence of embolic plaques [6, 7]. Given the complexity of blood flow dynamics in CRAO, mathematical modeling can offer potential avenues in research and the development of new therapies.

*Correspondence to: Basuki Widodo (Email: b_widodo@matematika.its.ac.id).
Department of Mathematics, Sepuluh Nopember Institute of Technology, Surabaya, Indonesia

ISSN 2310-5070 (online) ISSN 2311-004X (print)

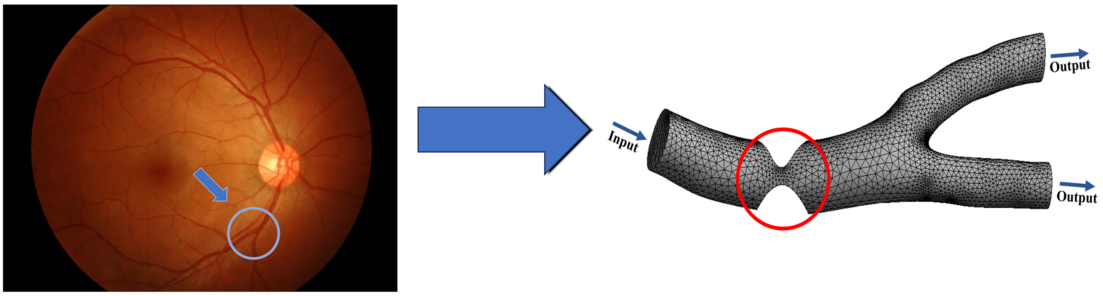

Figure 1. 3D Model of Retinal Artery [8].

Through mathematical models, researchers can represent the dynamics of blood flow in the retinal artery and identify factors contributing to occlusion [9, 10]. These models help in understanding the underlying pathological processes of CRAO and in evaluating the effectiveness of various therapeutic interventions. The mathematical models used in CRAO research typically involve the Navier-Stokes equations to describe blood flow in retinal tissues. Additionally, hemodynamic parameters such as blood flow velocity, viscosity, and arterial pressure are incorporated into the model to more accurately emulate physiological conditions [11, 12]. The numerical solutions of these mathematical models are carried out using the Finite Volume Method. This method is an effective discretization technique for partial differential equations, allowing for precise and stable numerical solutions of complex equations [13]. Using computer simulations, researchers can simulate various blood flow scenarios and evaluate the retinal tissue's response to different occlusion conditions [14, 15].

Previous research has extensively explored the impact of stenosis geometry on blood flow in vessels, with a focus on various geometric shapes and their influence on hemodynamics. Owasit and Sriyab [16] analyzed the mathematical model of vascular stenosis with bell-shaped and cosine-shaped geometries in arteries. Their study examined the effect of these shapes on blood flow velocity, presented in graphical form. Mwapinga et al. [17] focused on a mathematical model depicting stenosis with elliptical geometry. Simulations were conducted using MATLAB to study the characteristics of blood flow. Ellahi et al. [18] described a simulation model of vascular stenosis with circular geometry, providing insights into the effect of circular shape on blood flow in narrowed vessels. In the same vein, Hussain et al. [19] discussed a mathematical model for three types of stenosis geometries: triangular, elliptical, and trapezoidal. Their research analyzed the velocity, pressure, and temperature of blood for each geometric shape, with simulations performed using Fluent software. Tripathi and Sharma [20] focused on elliptical arterial stenosis that narrows due to radiation and chemical effects. This study presented mathematical models in the form of velocity contours and graphs to illustrate the results. Ponalagusamy and Machi [21] conducted an analysis of a mathematical model of arterial stenosis with six types of shapes: symmetric, triangular, trapezoidal, elliptical, bell-shaped, and composite. This research enriched the understanding of stenosis shape variations and their impact on blood flow. Kumar and Kumar [22] evaluated blood flow patterns in arteries with symmetrical, trapezoidal, triangular, cosine-shaped, and bell-shaped stenoses. Their analysis also involved heat transfer studies, using MATLAB to solve the system of equations.

This study builds upon the previous research by Hayreh (2011), Owasit and Sriyab (2021), as well as Kumar and Kumar (2023). The focus of this research is to develop a mathematical model and numerical simulation to analyze the impact of asymmetric stenosis on blood flow in the central retinal artery. By taking into account the effects of asymmetrical geometry, this study aims to provide a deeper understanding of blood flow dynamics, pressure distribution, and how these factors influence retinal tissue perfusion in cases of retinal artery occlusion. The aforementioned study primarily investigated the geometry of symmetric stenosis, whereas this study focuses on the geometry of asymmetric stenosis in cases of CRAO. Stenosis geometries vary based on what different patients experience [16]. The geometric shapes to be examined in this study are bell shape, cosine shape, and elliptical shape [22], with the stenosis located in the Central Retinal Artery [4]. Based on the literature, this study hypothesizes that the shape and thickness of the stenosis affect blood flow velocity and pressure in narrowed eye arteries. In the current analysis, we have numerically evaluated blood flow in cases of CRAO. The analysis is based on blood flow

through asymmetric stenosis geometries: Bell-Cosine Shape, Cosine-Elliptical Shape, and Bell-Elliptical Shape. The overall problem is formulated by considering a Cartesian coordinate system. The graphical solution includes a detailed analysis of flow velocity profiles, pressure profiles, contour pressures, and streamline patterns for all artery cases considered in the stenotic segment.

2. Materials and methods

2.1. Mathematical Formulation

The first step in this research is to formulate the CRAO problem mathematically, focusing on modelling blood flow in the central retinal artery and the impact of occlusion on blood flow to the retina. In this study, the stenosis geometry has an asymmetric shape, resulting from a combination of Bell, Cosine, and Elliptical shape. These three shapes were chosen because they more accurately represent naturally occurring stenosis in human blood vessels, as they reflect a gradual stenosis that aligns with the actual physiological process. Stenosis typically does not have a sharp or square shape; instead, it tends to form a smooth, asymmetrical curve. This can be modeled using Bell, Cosine, or Ellipse shapes, as illustrated in Figure 2 [16, 23]. Many studies have employed these shapes, making it easier to compare the results across various studies through the use of similar geometries.

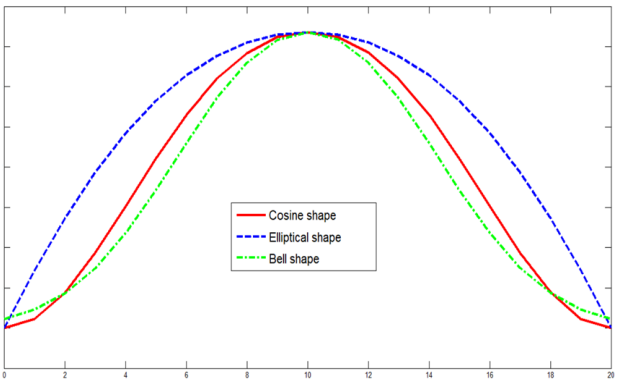

Figure 2. Geometry of stenosed artery with bell, cosine and elliptical shape.

The mathematical equations developed in this study are shown in Figure 3-5 below:

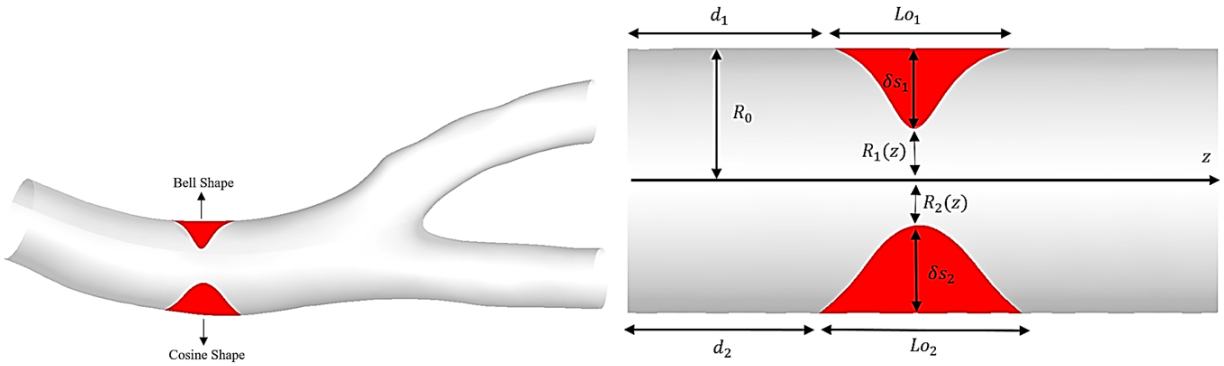

Figure 3. Schematic representation of model 12 (Bell-Cosine shape).

The mathematical equation used to account for the stenotic region of the artery, as given in Figure 3 (Model 12), includes the following stenotic wall function [16, 21, 22]:

$$\left.\begin{aligned} R_1(z) &= R_0 - \delta_s e^{-\frac{m^2}{R_0^2}\left(z-d_1-\frac{L_{o1}}{2}\right)^2} && ; d_1 \le z \le d_1 + L_{o1} \\ R_2(z) &= R_0 - \tfrac{\delta_s}{2}\left(1+\cos\tfrac{2\pi}{L_{o2}}\left(z-d_2-\tfrac{L_{o2}}{2}\right)\right) && ; d_2 \le z \le d_2 + L_{o2} \\ R_{1,2}(z) &= R_0 && ; \textit{otherwise} \end{aligned}\right\} \tag{2.1}$$

Referring to Figure 4 (Model 23), the mathematical equation used to account for the stenotic region of the artery includes the following stenotic wall function [16, 21, 22]:

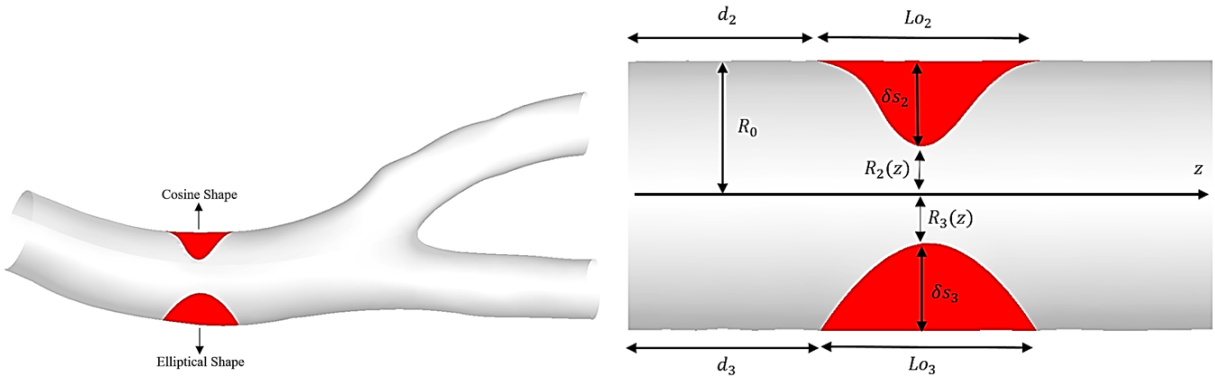

Figure 4. Schematic representation of model 23 (Cosine-Elliptical shape).

$$\left.\begin{aligned} R_2(z) &= R_0 - \tfrac{\delta_s}{2}\left(1+\cos\tfrac{2\pi}{L_{o2}}\left(z-d_2-\tfrac{L_{o2}}{2}\right)\right) && ; d_2 \le z \le d_2 + L_{o2} \\ R_3(z) &= R_0 - \delta_s \sin\left(\tfrac{\pi(z-d_3)}{L_{o3}}\right) && ; d_3 \le z \le d_3 + L_{o3} \\ R_{2,3}(z) &= R_0 && ; \textit{otherwise} \end{aligned}\right\} \tag{2.2}$$

As observed in Figure 5 (Model 13), the mathematical equation used to account for the stenotic region of the artery incorporates the following stenotic wall function [16, 21, 22]:

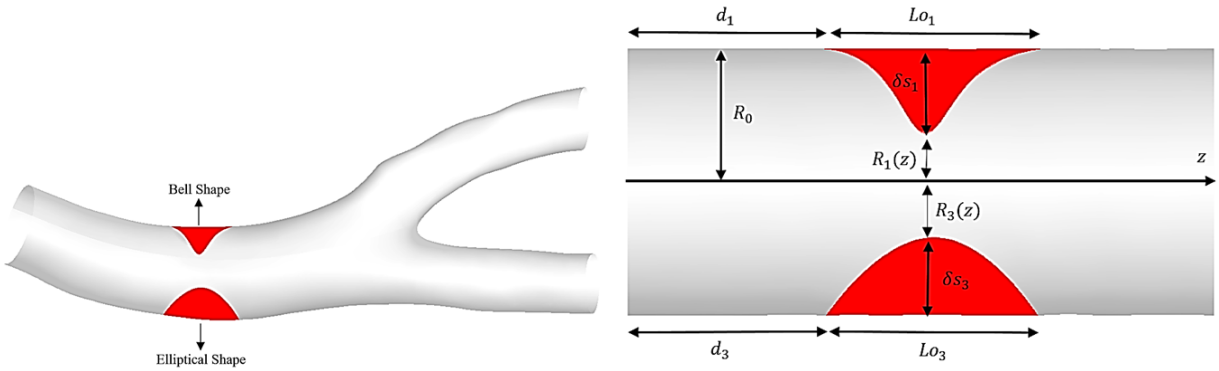

Figure 5. Schematic representation of model 13 (Bell-Elliptical shape).

$$\left.\begin{aligned} R_1(z) &= R_0 - \delta_s e^{-\frac{m^2}{R_0^2}\left(z-d_1-\frac{L_o}{2}\right)^2} && ; d_1 \le z \le d_1 + L_o \\ R_3(z) &= R_0 - \delta_s \sin\left(\tfrac{\pi(z-d_3)}{L_o}\right) && ; d_3 \le z \le d_3 + L_o \\ R_{1,3}(z) &= R_0 && ; \textit{otherwise} \end{aligned}\right\} \tag{2.3}$$

With:
$R_1(z)$ = the radius of a stenosed artery for Bell
$R_2(z)$ = the radius of a stenosed artery for Cosine
$R_3(z)$ = the radius of a stenosed artery for Elliptical
R_0 = the radius of a normal artery
δs_1 = the highest depth of the stenosis for Bell
δs_2 = the highest depth of the stenosis for Cosine
δs_3 = the highest depth of the stenosis for Elliptical
Lo_1 = the total length of the stenosis for Bell
Lo_2 = the total length of the stenosis for Cosine
Lo_3 = the total length of the stenosis for Elliptical
d_1 = stenosis location for Bell
d_2 = stenosis location for Cosine
d_3 = stenosis location for Elliptical
z = flow direction
L = the arterial length
m = parametric constant

This mathematical model was developed based on the Navier-Stokes equations to describe blood flow in the retinal tissue [9]. The Navier-Stokes equations are a system of nonlinear differential equations commonly used as the foundational equations in fluid mathematical modelling. The equation is utilized as a partial differential equation to solve a range of fluid flow problems [24]. The governing equations for this flow are given as follows:

$$\nabla \cdot \mathbf{V}_b = 0 \tag{2.4}$$

$$\frac{\partial \mathbf{V}_b}{\partial t} + \rho(\mathbf{V}_b \cdot \nabla \mathbf{V}_b) = -\nabla p + (\mu_f + \mu_s)\nabla^2 \mathbf{V}_b + \frac{\lambda}{2}\nabla(\nabla \cdot \mathbf{V}) \tag{2.5}$$

Correspondingly, the initial conditions are:

$$u(z,0) = u_0, \quad p(z,0) = P_0 \tag{2.6}$$

The boundary conditions are given as:

$$u(z,t) = 0, \quad v(z,t) = 0, \quad \frac{\partial u}{\partial z}(z,t) = 0 \quad \text{at } R = 0 \tag{2.7}$$

$$u(z,t) = \frac{\partial R}{\partial t}, \quad w(r,z,t) = 0 \quad \text{at } R = R(z,t) \tag{2.8}$$

The Neo-Hookean hyperelastic material model is adopted to simulate nonlinear stress-strain behavior for elastic materials subjected to large deformations, like blood vessels. The Cauchy stress tensor is given by [25, 26, 27, 28]:

$$\sigma_s = \frac{1}{J}F(\lambda(\text{tr}\mathbf{E})I + 2\mu_s\mathbf{E})F^T \tag{2.9}$$

where J is the determinant of the deformation gradient F, and λ and μ_s are the Lamé parameters, which depend on the Young's modulus E and Poisson's ratio ν

$$\mu_s = \frac{E}{2(1+\nu)}, \quad \lambda = \frac{E\nu}{(1-2\nu)(1+\nu)} \tag{2.10}$$

The deformation gradient is defined as $F = I + \nabla L^s$, and the strain tensor as $\mathbf{E} = \frac{1}{2}(F^T F - I)$, allowing the model to accommodate large deformations. The waveforms of the pulsatile pressure $P(t)$, are derived from Fourier series to represent temporal variations in pressure [29].

$$P(t) = \dot{P} + \sum_{i=1}^{4} A_i^P \cos(\iota\omega t) + B_i^P \sin(\iota\omega t) \tag{2.11}$$

This Fourier series represents periodic variations in flow and pressure that interact with the elastic properties of the material, producing a realistic stress response. The literature reveals a wide range of elastic properties for arteries. Some studies illustrate that tissues with soft behavior are characterized by a lower elastic modulus, while arteries with high stiffness exhibit a higher elastic modulus [29].

Table 1 presents the factors influencing blood flow rates in CRAO due to vascular narrowing [30, 31, 32, 33, 34]. Numerical experiments were conducted for flow through stenotic arteries with blockage variations and volume reductions of 45% – 90%.

Table 1. Values of parameters affecting blood flow rates in CRAO.

Parameter	**Value**
Diameter retinal artery	153.8 – 154.4 µm
Length stenosis	80 – 140 µm
Blood density	1.054 – 1.060 kg/m^3
Viscosity	0.003 kg/ms
Hypertensive blood pressure	Systolic: >140 mmHg Diastolic: >90 mmHg
Velocity artery	0.19 – 0.49 m/s
Initial Velocity	0.2 m/s
Pressure inlet	13332 Pa
Modulus young	0.3 – 1 MPa
Thermal Conductivity	0.44 W/mK

After identifying the values of the parameters that influence the blood flow rate in Central Retinal Artery Occlusion (CRAO), the Reynolds number will be calculated using the following formula to determine the type of flow present in the CRAO case:

$$Re = \frac{\rho U D}{\mu} \tag{2.12}$$

where U is the flow velocity (m/s), D the diameter of the cylinder (m), ρ the fluid density (kg/m^3), and μ the dynamic viscosity of the fluid (Ns/m^2). Based on Table 1, the Reynolds number calculation yields a value of 21.7, which indicates that the blood flow in Central Retinal Artery Occlusion (CRAO) is laminar. A Reynolds number smaller than 2000 suggests that the blood flow in CRAO does not experience turbulence. This laminar flow means that the fluid moves in parallel layers without mixing, resulting in stable and orderly flow.

2.2. Methodology

The present study employed MATLAB and the SIMPLE algorithm to solve the partial differential equations. The SIMPLE algorithm is a numerical procedure commonly used in Computational Fluid Dynamics (CFD) to address the fundamental equations of fluid flow [3]. The techniques employed in the SIMPLE algorithm included the Euler method for time integration of differential equations and the finite difference discretization method for approximating spatial derivatives in the Navier-Stokes equations. The steps of the SIMPLE algorithm are as follows [35]:

1. Determine the initial guesses for p^*, u^*, v^* and ϕ^*.

2. Solve the discretized momentum equations:

$$a_{l,j}u^*_{l,j} = \sum a_{nb}u^*_{nb} + \left(p^*_{l-1,j} - p^*_{l,j}\right) A_{l,j} + b_{l,j} \tag{2.13}$$

$$a_{l,j}v^*_{l,j} = \sum a_{nb}v^*_{nb} + \left(p^*_{l,j-1} - p^*_{l,j}\right) A_{l,j} + b_{l,j} \tag{2.14}$$

3. Solve the pressure correction equations:

$$a_{l,j}p'_{l,j} = a_{l+1,j}p'_{l+1,j} + a_{l-1,j}p'_{l-1,j} + a_{l,j+1}p'_{l,j+1} + a_{l,j-1}p'_{l,j-1} + b'_{l,j} \tag{2.15}$$

4. Determine the actual pressure and velocity:

$$u'_{l+1,j} = u^*_{l,j} + d^+_{l+1,j}(p'_{l,j} - p'_{l+1,j}) \tag{2.16}$$

$$v'_{l,j+1} = v^*_{l,j} + d^+_{l,j+1}(p'_{l,j} - p'_{l,j+1}) \tag{2.17}$$

5. Solve all other discretized transport equations:

$$a_{I,J}\phi_{I,J} = a_{I+1,J}\phi_{I+1,J} + a_{I-1,J}\phi_{I-1,J} + a_{I,J+1}\phi_{I,J+1} + a_{I,J-1}\phi_{I,J-1} \tag{2.18}$$

6. Check if the discretized solution has converged, if not repeat steps 1-4 until convergence is achieved.

MATLAB was used to develop and test this SIMPLE algorithm, ensuring that the generated numerical solutions were consistent and stable [9]. Subsequently, the simulation results were compared with ANSYS Fluent to validate the accuracy of the model. Comparing the results from both platforms enabled the demonstration of how MATLAB, despite using a simpler approach. This approximated the outcomes obtained from ANSYS Fluent, renowned for its advanced CFD processing capabilities. This comparison will focus on crucial aspects such as pressure distribution, flow velocity, and fluid behavior around the stenotic region. Validation is essential to ensure that the SIMPLE algorithm developed in MATLAB provides sufficiently accurate solutions prior to its application in more complex cases [36].

3. Results and Discussion

The MATLAB simulation results are compared with ANSYS Fluent to validate the model and assess the performance of the SIMPLE algorithm in capturing blood flow dynamics through stenotic arteries with three geometric shapes (Bell-Cosine, Cosine-Elliptical, and Bell-Elliptical). The comparison focuses on flow velocity and pressure distribution. Based on Figure 5, the velocity profiles from both platforms exhibit similar trends, with the highest velocity observed at the center of the stenosis, particularly in the Cosine-Elliptical shape. However, ANSYS shows sharper velocity gradients, especially for 90% stenosis, likely due to finer meshing and more advanced turbulence models. Velocity distribution graphs highlight differences between normal and critical flow conditions. For stenosis levels between 45% to 60%, the flow remains stable. However, at 75% to 90% stenosis, the velocity increases sharply, exceeding normal limits (>0.5 m/s), indicating a transition to disturbed flow, potentially leading to clinical complications. The 90% stenosis condition is the most critical, with the highest velocity peaks and significant flow disturbances. Among the three models, the Cosine-Elliptical shape generates the highest velocity, posing the greatest risk of turbulence and shear stress on vessel walls, making it the most prone to severe hemodynamic complications.

Based on the pressure comparison for each model, Figure 6(a) shows that elevated degree of stenosis results in a more significant pressure drop, especially at the maximum stenosis point. Figure 6(b-d) confirm that the simulation results from MATLAB generally align with those from ANSYS Fluent. However, in cases of more severe stenosis (75% and 90%), ANSYS Fluent tends to show a sharper pressure drop compared to MATLAB, particularly around the stenosis area. This discrepancy is likely due to differences in how the numerical models or physical parameters are handled in the two software platforms. Overall, the figures show that while there are minor differences in

pressure distribution between the two geometric approaches used in MATLAB and the results from ANSYS Fluent, both simulations exhibit consistent trends, with increasing degrees of stenosis leading to a more substantial drop around the narrowing region. Based on Figure 6, the pressure distribution shows a significant decrease in the stenotic region, with the most critical condition occurring at the 90% stenosis level, where the pressure reaches its lowest value. This sharp drop indicates severe hemodynamic effects, including increased turbulence, high shear stress, and a higher risk of vessel collapse. As the stenosis severity increases from 75% to 90%, the pressure drop becomes more pronounced, especially in the Cosine-Elliptical and Bell-Elliptical shapes, indicating a transition from normal to disturbed flow conditions.

Based on the pressure comparison for each model, Figure 7(a) shows that elevated degree of stenosis results in a more significant pressure drop, especially at the maximum stenosis point. Figure 7(b-d) confirm that the simulation results from MATLAB generally align with those from ANSYS Fluent. However, in cases of more severe stenosis (75% and 90%), ANSYS Fluent tends to show a sharper pressure drop compared to MATLAB, particularly around the stenosis area. This discrepancy is likely due to differences in how the numerical models or physical parameters are handled in the two software platforms. Overall, the figures show that while there are minor differences in pressure distribution between the two geometric approaches used in MATLAB and the results from ANSYS Fluent, both simulations exhibit consistent trends, with increasing degrees of stenosis leading to a more substantial drop around the narrowing region.

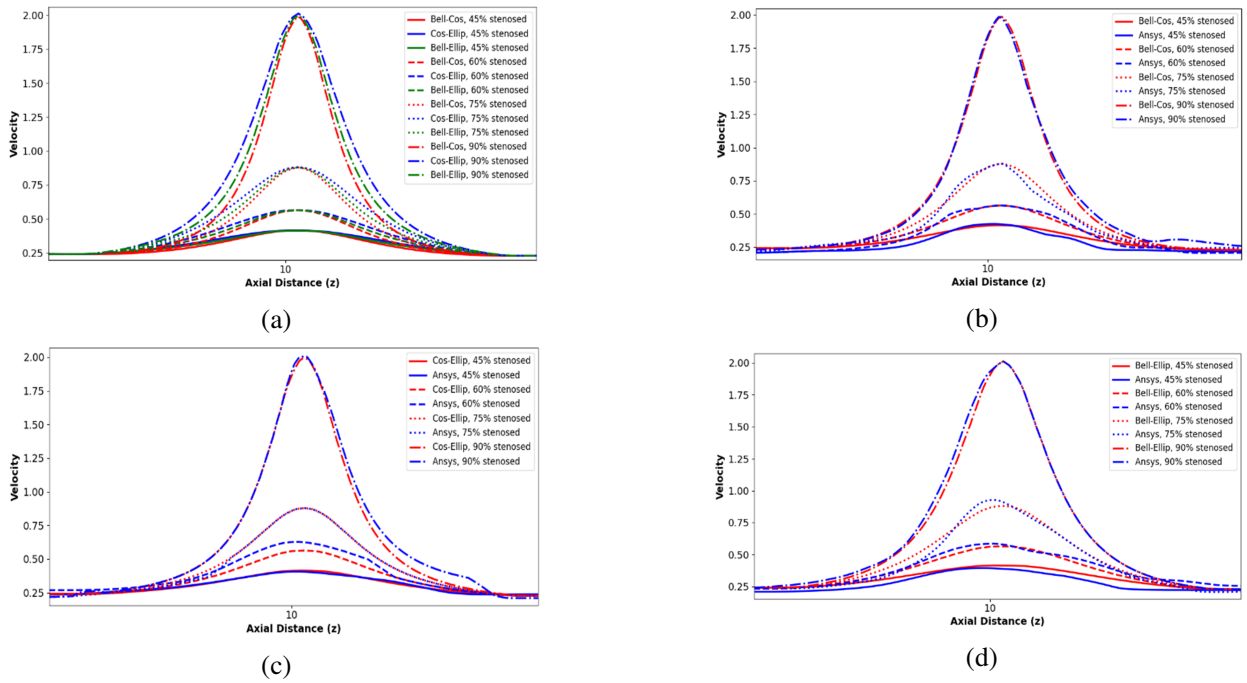

Figure 6. Comparison of axial flow velocity: (a) all models, (b) Bell-Cosine model with ANSYS simulation, (c) Cosine-Elliptical model with ANSYS simulation, (d) Bell-Elliptical model with ANSYS simulation.

The comparison between MATLAB and ANSYS Fluent demonstrates that the MATLAB model using the SIMPLE algorithm is capable of producing accurate and reliable results for blood flow through stenotic arteries. While there are minor differences in the sharpness of the velocity gradients and pressure drops, the general trends in flow velocity, and pressure distribution are consistent between the two platforms. These results validate the use of MATLAB for further analysis and suggest that it provides a computationally efficient alternative to ANSYS for simulating fluid flow in stenotic arteries. After comparing the simulation results between MATLAB and ANSYS, mesh independence tests were conducted to ensure the accuracy and reliability of the computational results. This test involved varying the mesh size and evaluating the peak velocity and pressure drop at different mesh resolutions.

Three mesh sizes (coarse, medium, and fine) were used to observe the impact of mesh refinement on the results. The comparison of peak velocity and peak pressure between the MATLAB and ANSYS results at each mesh size is shown in Table 2-4, with the percentage differences calculated to assess the convergence of the solution.

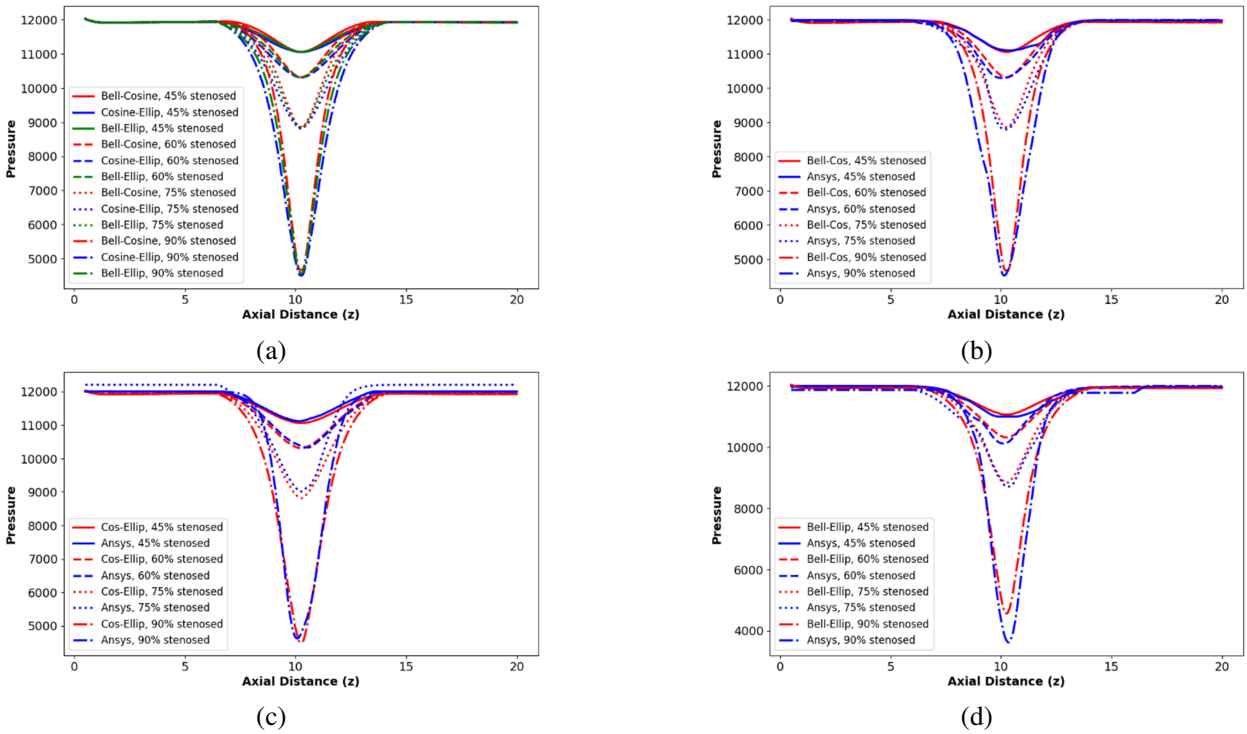

Figure 7. Comparison of pressure: (a) all models, (b) Bell-Cosine model with ANSYS simulation, (c) Cosine-Elliptical model with ANSYS simulation, (d) Bell-Elliptical model with ANSYS simulation.

Table 2. Comparison of Peak Velocity and Peak Pressure for Bell-Cosine Stenosis at Different Mesh Sizes.

Mesh Size	**Number of Nodes**	**Peak Velocity**		**%Difference**	**Peak Pressure Drop**		**%Difference**
		MATLAB	**ANSYS**		**MATLAB**	**ANSYS**	
Coarse Mesh	75702	0.913	0.97	6.05%	8687.288	9187.58	5.59%
Medium Mesh	163891	0.883	0.916	3.66%	8691.350	8977.76	3.24%
Fine Mesh	309720	0.855	0.863	0.93%	8779.575	8890.59	1.25%

Table 3. Comparison of Peak Velocity and Peak Pressure for Cosine-Elliptical Stenosis at Different Mesh Sizes.

Mesh Size	**Number of Nodes**	**Peak Velocity**		**%Difference**	**Peak Pressure Drop**		**%Difference**
		MATLAB	**ANSYS**		**MATLAB**	**ANSYS**	
Coarse Mesh	75702	0.915	0.985	7.36%	8683.365	9243.365	6.24%
Medium Mesh	163891	0.884	0.924	4.42%	8689.256	8989.256	3.39%
Fine Mesh	309720	0.856	0.866	1.16%	8777.412	8893.412	1.31%

Table 4. Comparison of Peak Velocity and Peak Pressure for Bell-Elliptical Stenosis at Different Mesh Sizes.

Mesh Size	Number of Nodes	Peak Velocity MATLAB	Peak Velocity ANSYS	%Difference	Peak Pressure Drop MATLAB	Peak Pressure Drop ANSYS	%Difference
Coarse Mesh	75702	0.913	0.973	6.36%	8685.368	9185.368	5.59%
Medium Mesh	163891	0.884	0.919	3.88%	8689.873	8970.873	3.18%
Fine Mesh	309720	0.855	0.865	1.16%	8777.951	8897.951	1.35%

From the results of the mesh independence test shown in Tables 2-4, it can be analyzed that the accuracy of the calculations for peak velocity and peak pressure drop in the three stenosis models tends to improve with increasing mesh resolution. The percentage differences between the MATLAB and ANSYS calculation results show that as the mesh becomes finer, the differences between the two software programs decrease. This indicates that the calculations are converging as the mesh is refined. Similarly, the difference in pressure drop also shows a reduction in the percentage difference with increased mesh resolution. Based on these results, it can be concluded that a finer mesh provides a more stable and reliable solution for flow simulations in the stenosis models. Therefore, based on the mesh independence test results, to ensure the accuracy of the simulation outcomes, a finer mesh should be used, although the increased accuracy will require more computational resources.

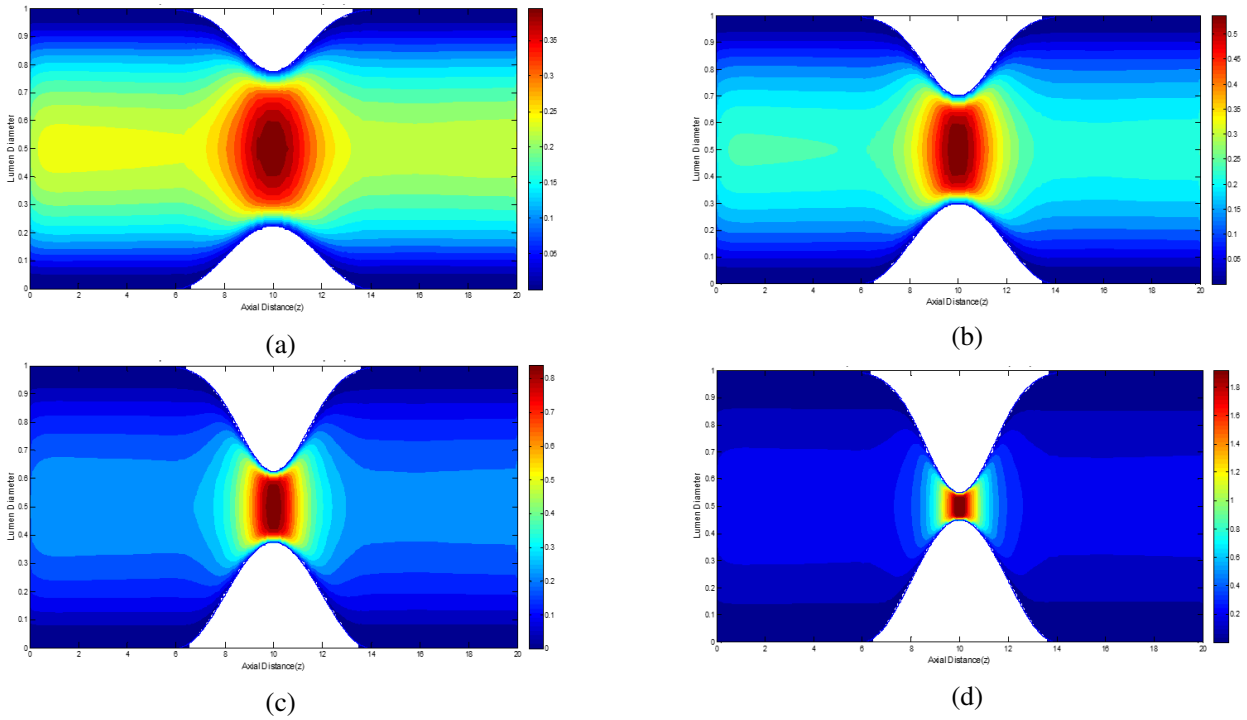

Figure 8. Velocity contours for different stenosis thicknesses in the asymmetric Bell-Cosine shape geometry: (a) 45% stenosis (b) 60% stenosis (c) 75% stenosis (d) 90% stenosis.

The solution to this problem was addressed numerically using MATLAB software. In the Finite Volume Method (FVM), the entire domain was discretized into a set of small control volumes (known as cells), and the differential equations were integrated into these cells. The simulation results in Figure 8 display the fluid flow velocity distribution in a stenosis model with a Bell-Cosine shape, where the thickness of the stenosis varies. As the level of vessel narrowing increased from 45% to 90%, the area available for fluid flow significantly narrowed. This results

in drastic changes in velocity distribution along the vessel at the stenosis point, ranging from 0.42 m/s for a 45% narrowing to 2.01 m/s for a 90% narrowing.

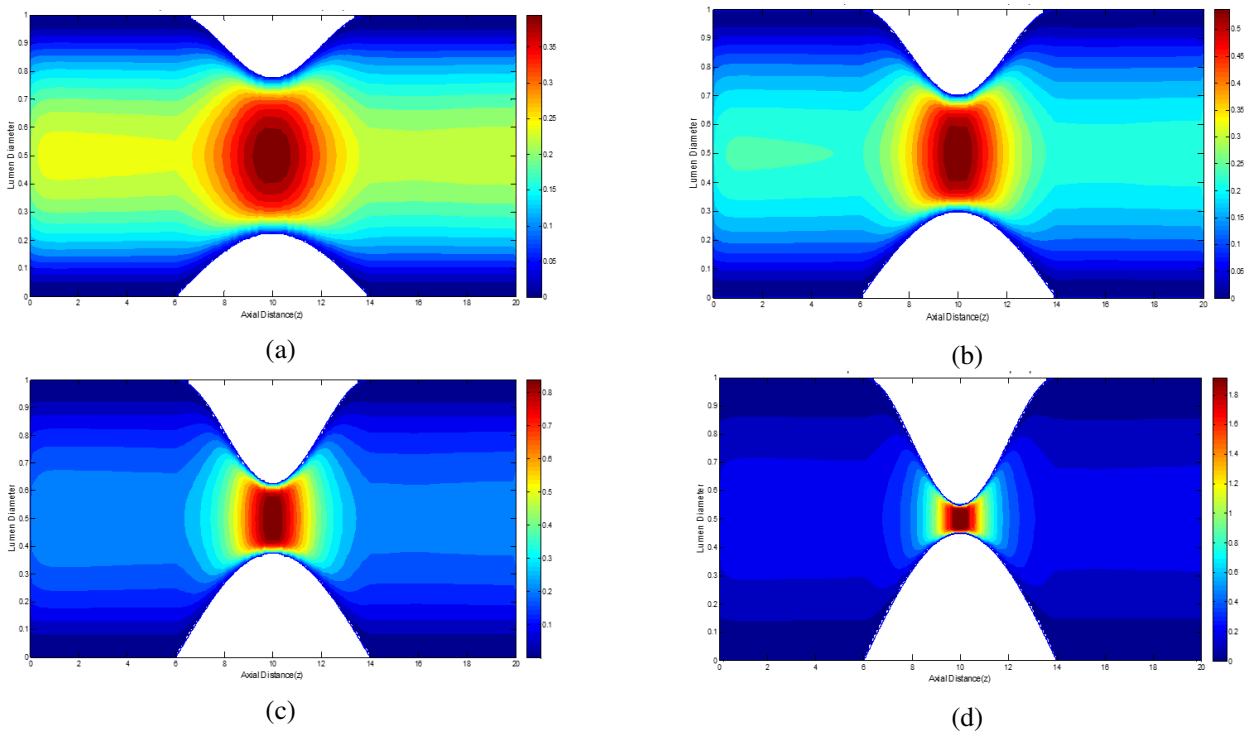

Figure 9. Velocity contours for different stenosis thicknesses in the asymmetric Cosine-Eliptical shape geometry: (a) 45% stenosis (b) 60% stenosis (c) 75% stenosis (d) 90% stenosis.

Based on Figure 8, it is evident that the highest fluid flow velocities occur in Figure 8c and 8d, where the velocities at the center of the stenosis are 0.86 m/s and 2.01 m/s, respectively. Under these conditions, the fluid experiences a phenomenon known as ”jetting,” where the fluid is forced to pass through a narrow area at a very high velocity. This phenomenon creates a zone of extreme fluid velocity after passing through the stenosis area, which could potentially damage the vessel walls if this condition persists. The jetting phenomenon is a critical indicator to monitor, as it may escalate the risk of serious complications in the cardiovascular system.

The simulation results in Figure 9 illustrate the fluid flow velocity distribution in a stenosis model with a Cosine-Elliptical shape, where the thickness of the stenosis varies. As the vessel narrowing increases from 45% to 90%, a pronounced pattern emerges, with areas of high velocity (represented by red to yellow colors) becoming increasingly concentrated at the center of the stenosis. At 90% narrowing, the velocities concentrate in the stenosis center within the range of 0.2 m/s to 2.02 m/s. This indicates a significant increase in the velocity gradient along the flow. At the levels of narrowing of 75% and 90%, the fluid flow velocities at the center of the stenosis reach 0.88 m/s and 2.02 m/s, respectively, leading to the jetting. This phenomenon becomes more pronounced, especially in Figure 9c and 9d, indicating a greater potential risk to the vessel walls due to the very rapid flow.

The simulation results in Figure 10 depict the fluid velocity distribution within the blood vessels, with increasing degrees of stenosis in the Bell–Elliptical shaped model. The results align with previous models, showing that as the stenosis thickness increases from 45% to 90%, areas of high velocity (represented by red to yellow colors) emerge and concentrate in the stenosis center, ranging from 0.41 m/s to 2.01 m/s. In Figure 10d, which illustrates the highest degree of stenosis, the ”jetting” becomes more prominent. The fluid is forced through a narrow gap at extremely high speeds, creating significant pressure on the vessel walls, which can increase the local pressure downstream of the stenosis. This elevated pressure can result in additional stress on the blood vessel walls, potentially leading

to vessel wall damage and an increased risk of rupture. This phenomenon underscores the importance of early monitoring and intervention in severe stenosis conditions.

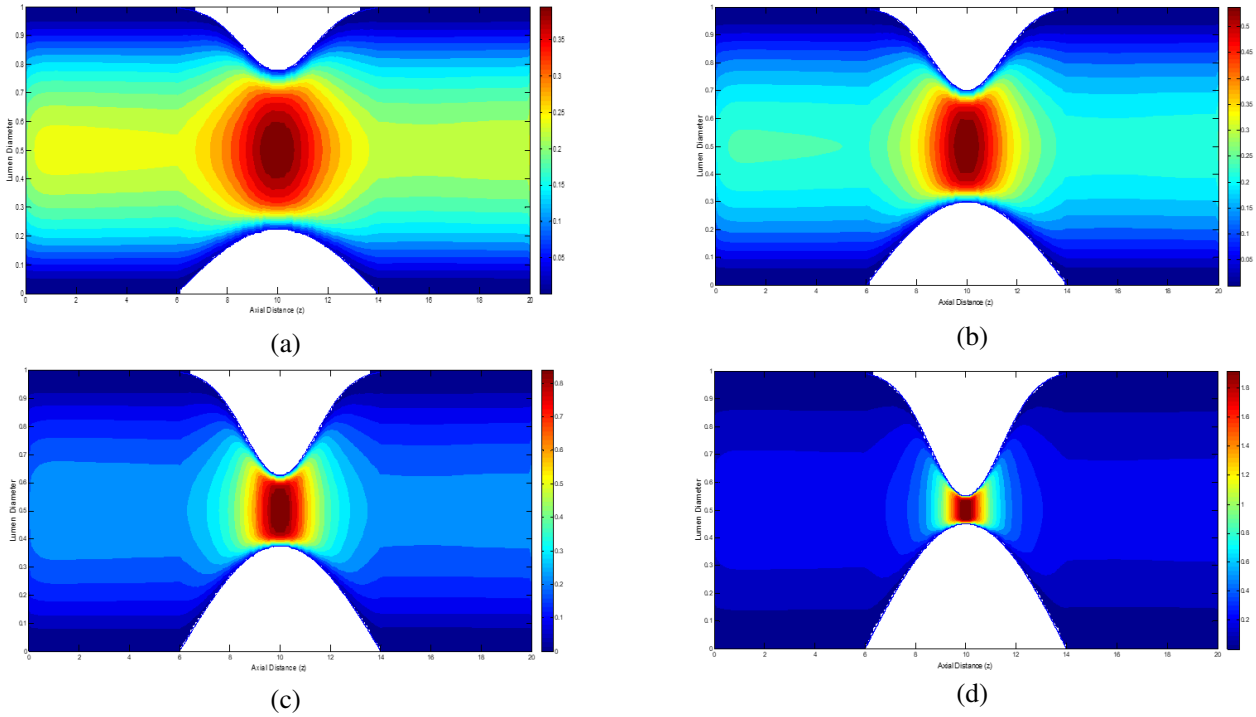

Figure 10. Velocity contours for different stenosis thicknesses in the asymmetric Bell-Elliptical shape geometry: (a) 45% stenosis, (b) 60% stenosis, (c) 75% stenosis, and (d) 90% stenosis.

In the subsequent simulation, the effects of stenosis position on flow rate are examined across three models. The simulation results in Figure 11 show the velocity distribution with varying stenosis positions in the Bell-Cosine shaped model (60% stenosis) with a narrowing length of $Lo_1 = Lo_2 = 8$. In Figure 11b, laminar flow occurs in just one region at the center of the stenosis, with a very high velocity distribution (indicated by the red color), measuring 0.56 m/s. Figure 11a and 11c display two stenosis points with a more complex velocity distribution pattern. In these figures, two zones of high-velocity laminar flow are generated by two different stenosis locations. This phenomenon creates a broader velocity distribution, ranging from 0.23 m/s to 0.34 m/s. This indicates that varying stenosis positions result in a more uniform velocity distribution compared to stenosis in the same location. Figure 11d presents the velocity profile along the axial distance (z) for various combinations of d_1 and d_2 values. The graph shows that positional differences (d_1 and d_2) lead to distinct variations in peak velocity within the stenosis zone. A greater difference between d_1 and d_2 results in a lower peak velocity in the stenosis area and leads to the appearance of two laminar flows around the stenosis region.

The simulation results in Figure 12 illustrate the fluid velocity distribution with varying stenosis positions in the Cosine-Elliptical shaped model (60% stenosis) with a narrowing length of $Lo_2 = Lo_3 = 8$. In Figure 12b, the stenosis creates a high-velocity area concentrated in the middle of the stenosis (represented by red to yellow colors), ranging from 0.2 m/s to 0.56 m/s. This velocity distribution demonstrates how the fluid flow focuses on a single stenosis point, creating a sharp velocity gradient after passing through the constriction. Meanwhile, Figure 12a and 12c show two stenosis areas producing two adjacent high-velocity zones. This phenomenon illustrates the complexity of fluid flow as it navigates through two narrow regions consecutively. The result is a more even velocity distribution, with speeds ranging from 0.21 m/s to 0.33 m/s. This finding is consistent with the results in Figure 11, where different stenosis positions lead to a more uniform velocity distribution compared to stenosis in the same location.

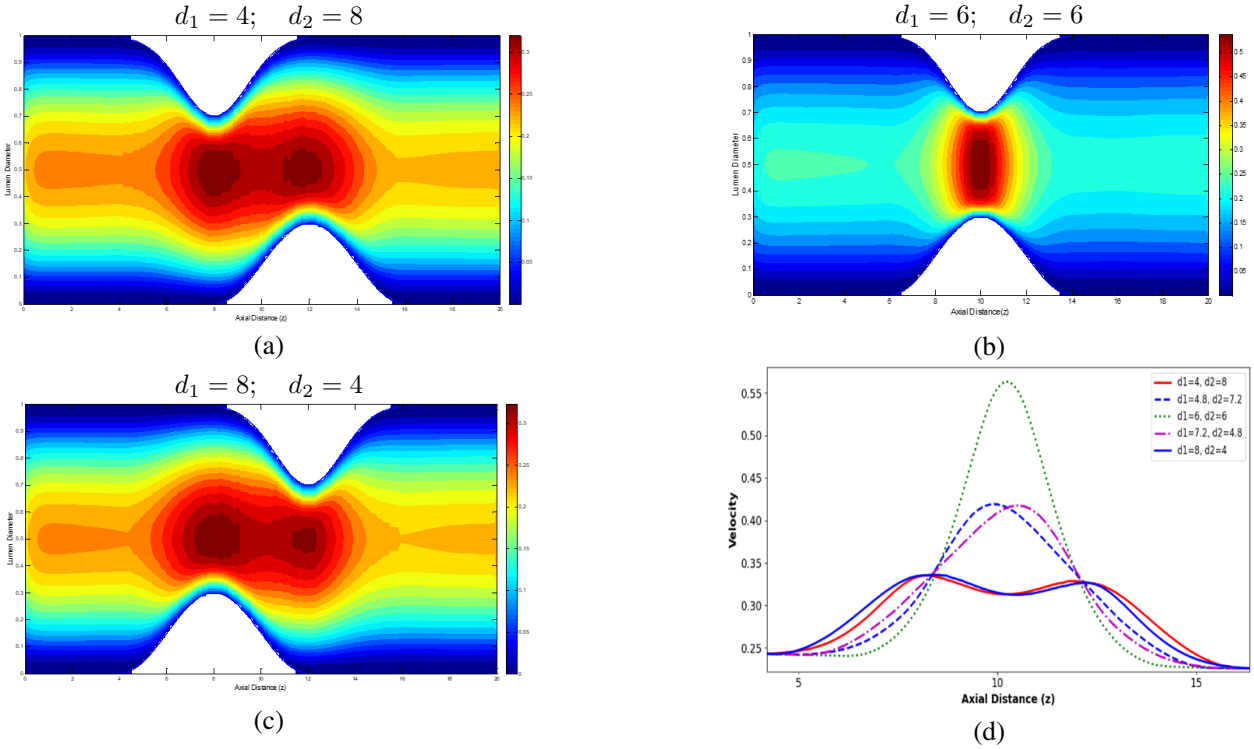

Figure 11. Velocity contours with varying stenosis positions for the asymmetric Bell-Cosine geometry shape.

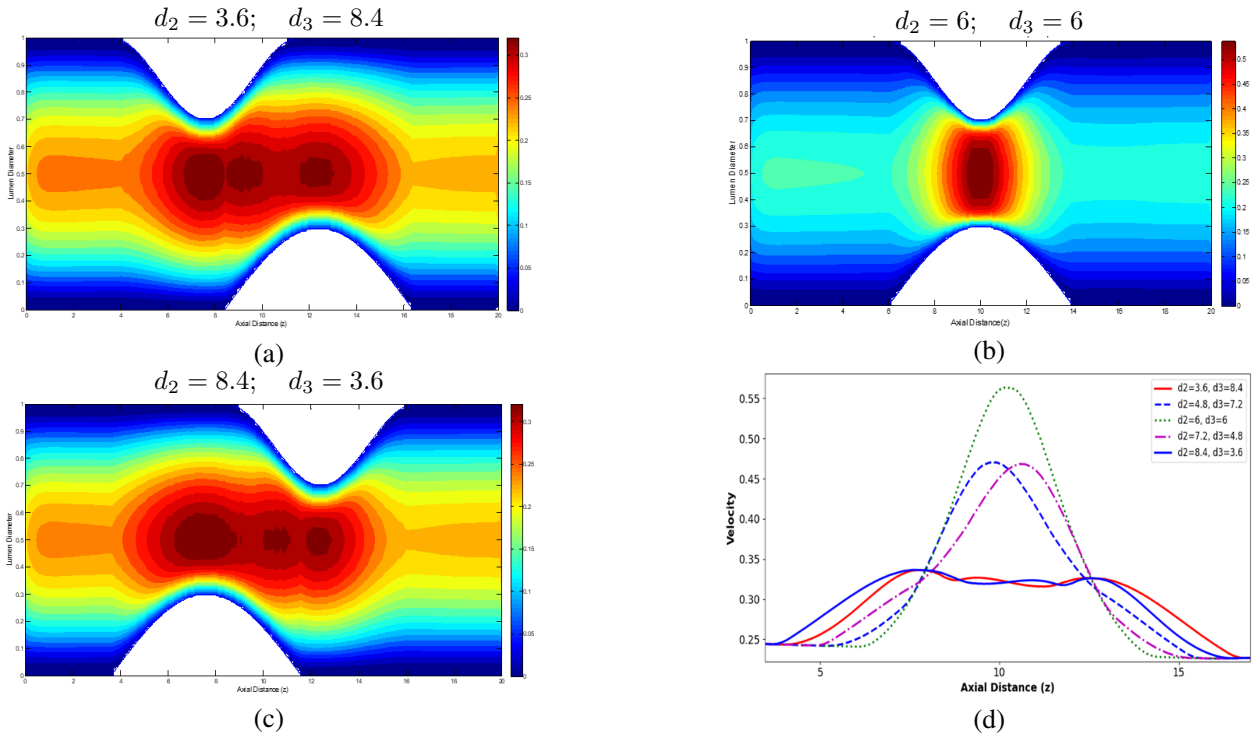

Figure 12. Velocity contours with varying stenosis positions for the asymmetric Cosine-Elliptical geometry shape.

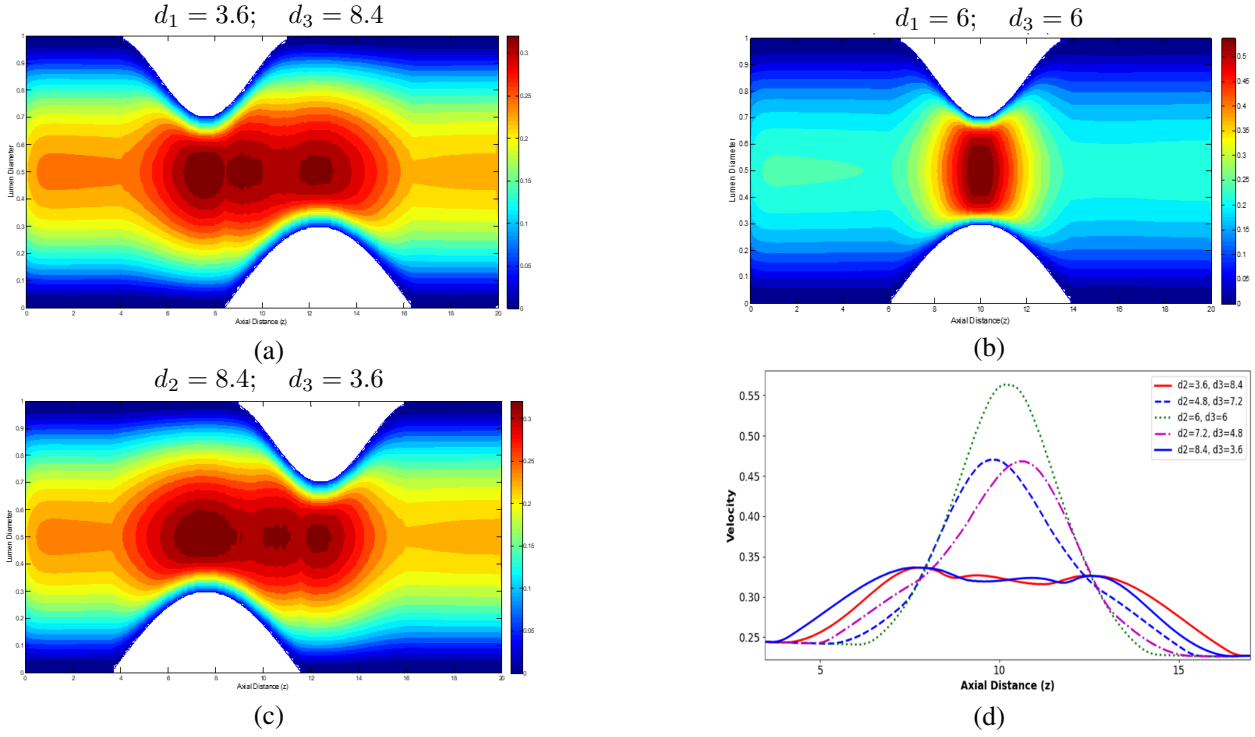

Figure 13. Velocity contours with varying stenosis positions for the asymmetric Bell-Elliptical geometry shape.

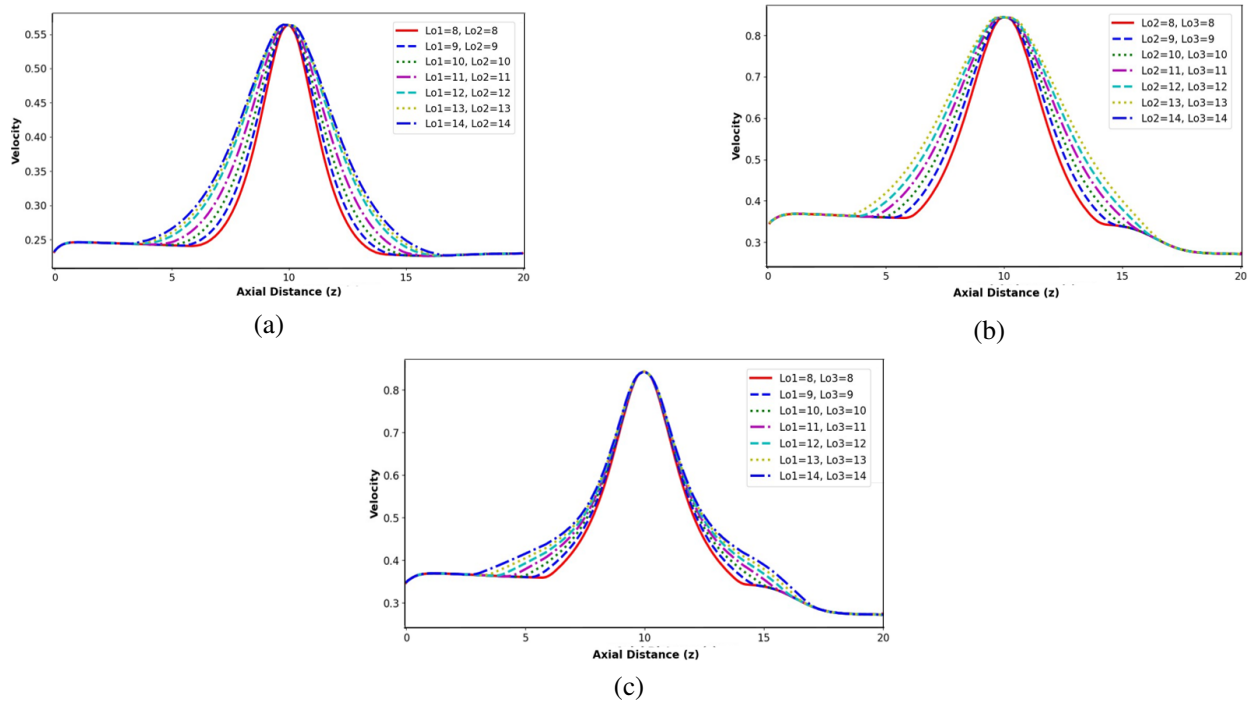

Figure 14. Flow velocity variation with different stenosis lengths for three asymmetrical shapes: (a) Bell-Cosine, (b) Cosine-Elliptical, (c) Bell-Elliptical.

The simulation results in Figure 13 illustrate the fluid velocity distribution with varying stenosis positions in the Bell-Elliptical shaped model (60% stenosis) with a narrowing length of $Lo_1 = Lo_3 = 8$. In Figure 13b, the stenosis occurs at a specific point, resulting in very high fluid velocity in the stenosis area (indicated by the red color), ranging from 0.24 m/s to 0.56 m/s. This velocity distribution demonstrates how the fluid is forced through a narrow gap, causing a significant increase in speed. Meanwhile, Figure 13a and 13c show double stenosis in the blood vessel. These two stenosis zones create two adjacent high-velocity areas, illustrating how the fluid flow must navigate through two narrow areas consecutively. This pattern results in a more uniform velocity distribution, ranging from 0.24 m/s to 0.35 m/s. This result is consistent with the findings in Figure 11 and 12, where different stenosis positions lead to a more uniform velocity distribution compared to stenosis in the same location.

The next simulation results demonstrate the effect of stenosis length on flow rate for each developed geometric shape. The simulation results in Figure 14 exhibit that varying the length of the stenosis does not significantly affect the flow velocity for each model. The highest flow velocity remains at the center of the stenosis for each model, while the stenosis length only widens the laminar region around the stenosis area by 30 – 60 μm on both sides of the curve along the axial distance (z).

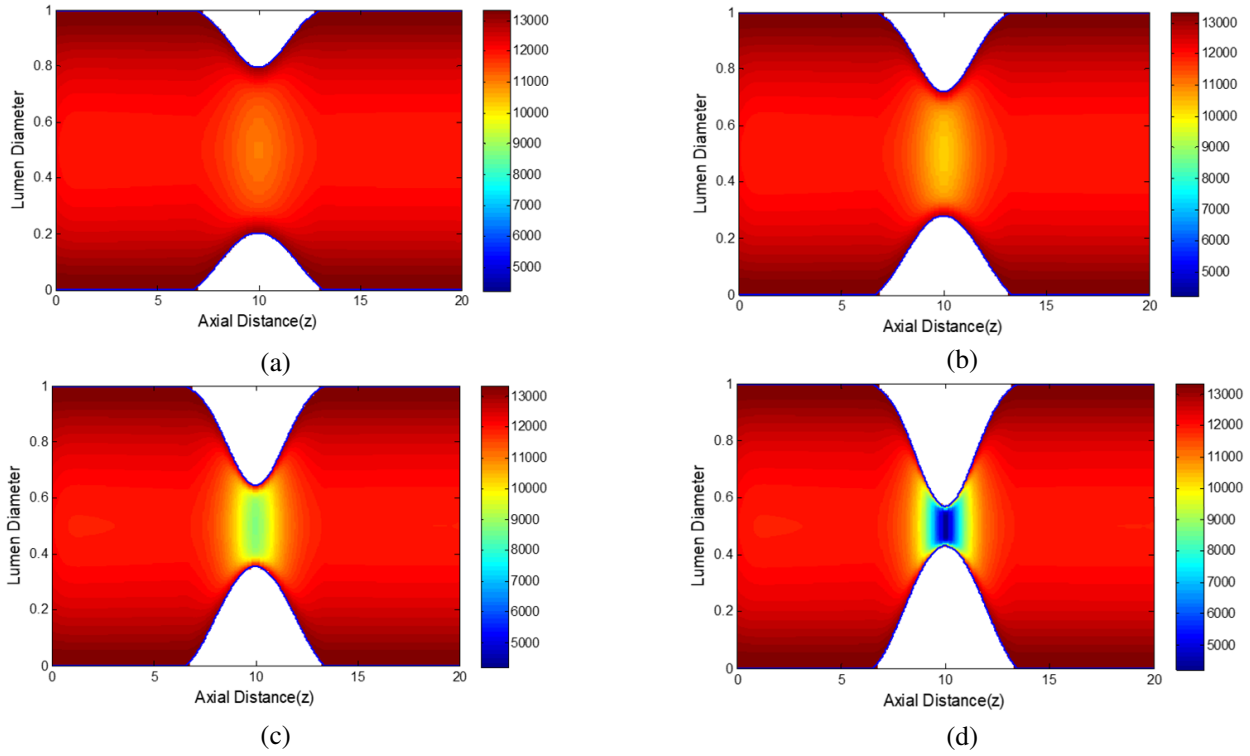

Figure 15. Pressure patterns for the asymmetric Bell-Cosine geometry shape: (a) 45% stenosis, (b) 60% stenosis, (c) 75% stenosis, (d) 90% stenosis.

The simulation results in Figure 15 show the pressure distribution of fluid flow in the stenosis model with a Bell-Cosine shape, where the stenosis thickness varies. As the degree of vessel narrowing increases from 45% to 90%, the area available for fluid flow narrows significantly. In Figure 15(a), the pressure distribution around the stenosis remains relatively balanced, with a clear pressure gradient around the narrowing, ranging from 8735 Pa to 13331 Pa. The blue area in the middle of the figure indicates a region of lower pressure around the stenosis, which is a common characteristic of narrowing in fluid flow. In fluid dynamics theory, the Venturi effect explains that when fluid passes through a constriction, its velocity increases while its pressure decreases. This is consistent with the figure, which shows a pressure drop in the stenosis region (marked in blue), where the acceleration of the flow causes a sharp decrease in static pressure. In Figure 15c and 15d, the pressure around the stenosis exhibits a

significant increase, which can be attributed to changes in the elasticity of the vessel walls or stiffness in the stenosis geometry, leading to a sharper pressure gradient. The extreme pressure drop, reaching values of 8780 Pa and 4226 Pa in both figures, indicates a sharp increase in pressure differences between the upstream and downstream regions of the stenosis.

The simulation results in Figure 16 show the fluid pressure distribution in the stenosis model with a Cosine-Elliptical shape, where the stenosis thickness varies. As the degree of vessel narrowing increases from 45% to 90%, the area available for fluid flow narrows significantly, leading to marked changes in pressure distribution. In Figure 16a, the pressure distribution around the stenosis remains relatively uniform, with a clear pressure gradient ranging from 11053 Pa to 13331 Pa. In Figure 16b, the pressure gradient ranges from 10295 Pa to 13331 Pa. The blue area in the center indicates a region of lower pressure compared to the surrounding areas. However, in Figure 16c and 16d, the pressure around the stenosis increases drastically. The low-pressure area intensifies, reaching values of approximately 8777 Pa and 4225 Pa. This elevated pressure difference underscores the impact of critical stenosis on fluid dynamics, especially marked decrease pressure as vessel narrows.

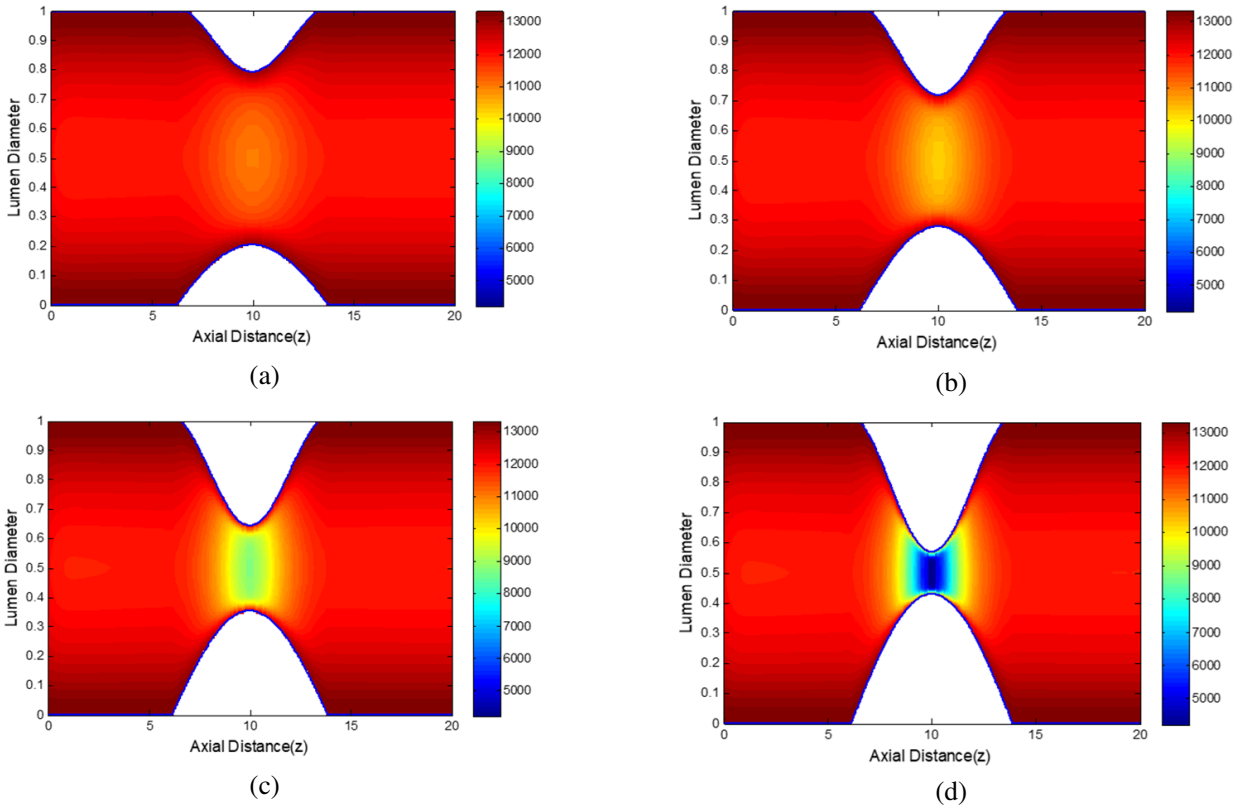

Figure 16. Pressure patterns for the asymmetric Cosine-Elliptical geometry shape: (a) 45% stenosis, (b) 60% stenosis, (c) 75% stenosis, (d) 90% stenosis

The simulation results in Figure 17 depict the fluid pressure distribution in the stenosis model with a Bell-Elliptical shape, where the stenosis thickness varies. As the degree of vessel narrowing increases from 45% to 90%, the area available for fluid flow narrows significantly. In Figure 17a, the pressure distribution around the stenosis area remains relatively uniform, with a clear pressure gradient ranging from 11054 Pa to 13331 Pa. In Figure 17b, the pressure gradient ranges from 10295 Pa to 13331 Pa. The blue area in the center indicates a region of lower pressure compared to the surroundings. However, in Figure 17c and 17d, the pressure around the stenosis increases drastically. The low-pressure area intensifies, with minimum pressure dropping to range between 8778 Pa and 4226 Pa.

The simulation results across different stenosis models (Bell-Cosine, Cosine-Elliptical, and Bell-Elliptical) show consistent trends as the degree of vessel narrowing increases from 45% to 90%. As the stenosis thickens, the available area for fluid flow decreases, leading to significant pressure changes. In all models, a pressure drop occurs in the narrowed region due to the acceleration of the fluid, consistent with the Venturi effect. The pressure gradient becomes more pronounced as the narrowing increases, with extreme pressure drops observed at higher degrees of stenosis. This results in larger pressure differences between the upstream and downstream regions. These findings highlight the critical impact of stenosis geometry on fluid dynamics, where greater narrowing leads to more intense pressure variations, which can affect flow stability and system performance.

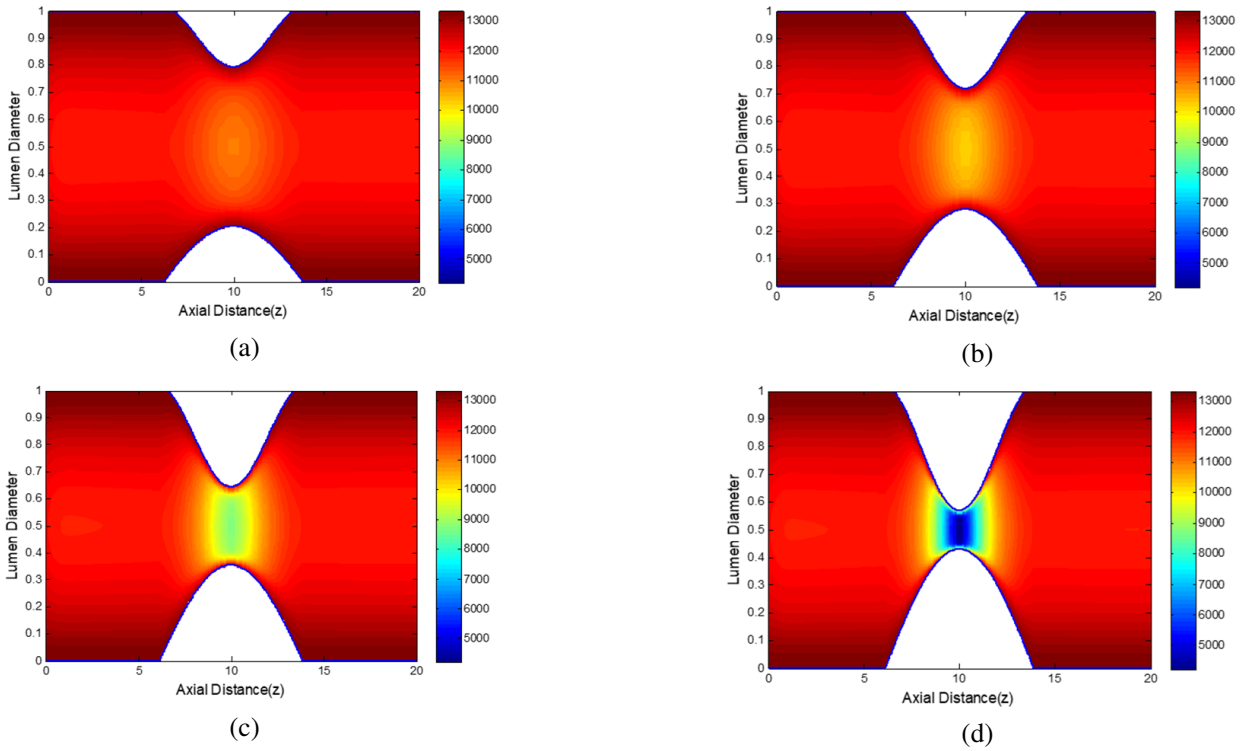

Figure 17. Pressure patterns for the asymmetric Bell-Elliptical geometry shape: (a) 45% stenosis, (b) 60% stenosis, (c) 75% stenosis, (d) 90% stenosis

Figure 18 illustrates the pressure variation along the axial distance for different stenosis positions in the Bell-Cosine shape stenosis model (60% stenosis) with a narrowing length of $Lo_1 = Lo_2 = 8$. The results show the pressure distribution contours for different stenosis configurations, with variations in stenosis positions. The color map indicates the pressure range, with red areas representing higher pressure values and blue areas indicating lower pressures. In all cases, the narrowing of the artery caused by stenosis elevates the pressure near the constricted regions, as indicated by the color gradients in the contours. As the flow moves through the stenosis, the pressure drops sharply due to the reduction in lumen diameter. In Figure 18b, it is shown that when the stenosis positions are the same, the pressure drops sharply to around 10294 Pa. Meanwhile, for different stenosis positions, as seen in Figure 18a and 18c, two areas of lower pressure appear, with values ranging from 11423 to 11437 Pa. The results indicate that stenosis position and the degree of narrowing significantly affect the pressure distribution along the artery. Figure 18d presents the quantitative pressure profile along the axial distance for various stenosis configurations. The pressure peaks near the stenosis area and drops sharply as the flow moves past the narrowing, followed by a gradual recovery. This profile shows that the placement and shape of the stenosis influence the overall flow characteristics, where configurations with a larger difference in stenosis positions d_1 = 8.4, d_2 = 3.6 or vice versa) result in a more pronounced pressure drop and a smoother recovery compared to other configurations.

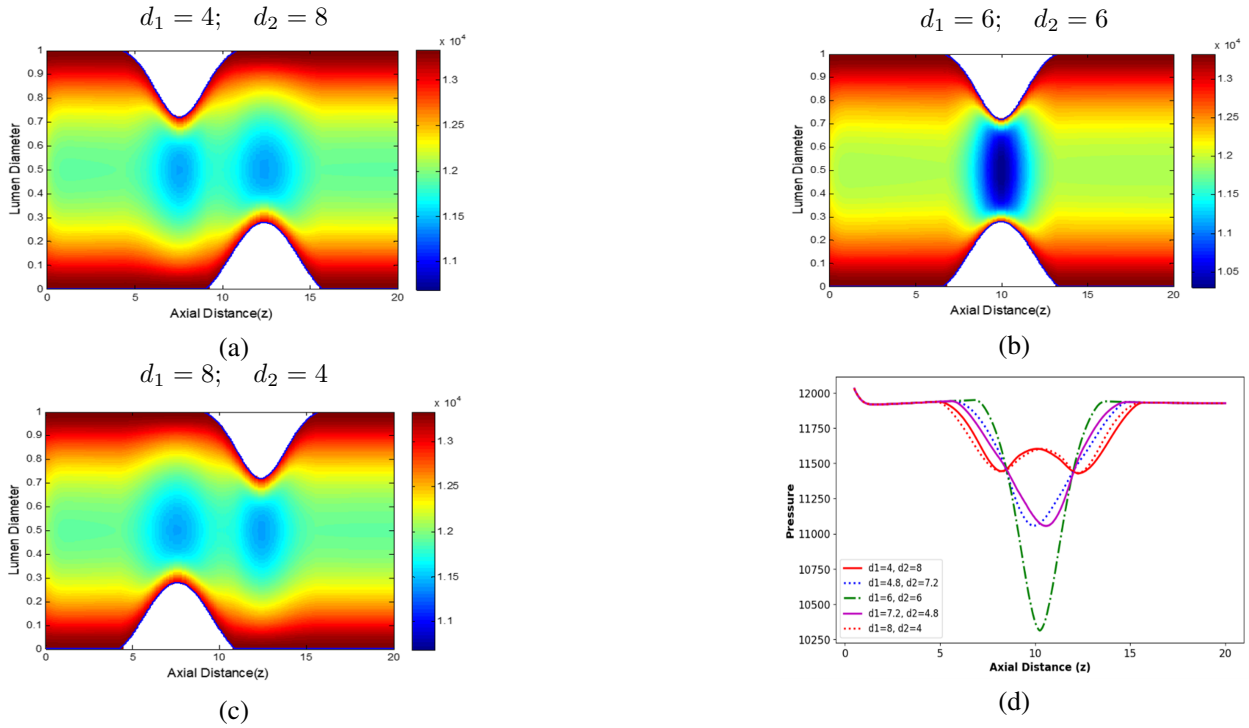

Figure 18. Pressure variation with axial distance for different stenosis positions in Bell-Cosine shape stenosis.

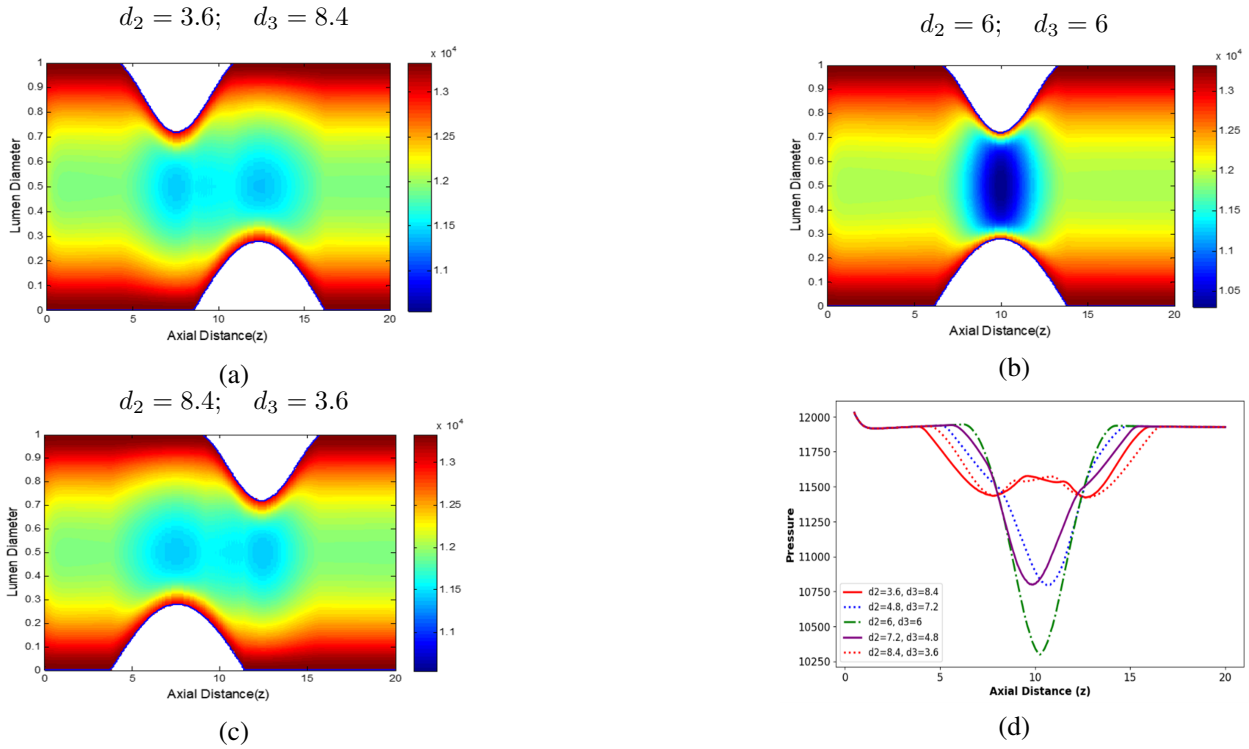

Figure 19. Pressure variation with axial distance for different stenosis positions in Cosine-Elliptical shape stenosis.

The simulation results in Figure 19 illustrate the fluid pressure distribution with varying stenosis positions in the Cosine-Elliptical shape model (60% stenosis) with a narrowing length of $Lo_1 = Lo_2 = 8$. Figure 19b shows the pressure distribution around the stenosed blood vessel (narrowing with low pressure, approximately 10295 Pa), clearly visible with the dominant blue color in the central area. Meanwhile, Figure 19a and 19c depict the pressure distribution along the blood vessel with two stenoses. The dark blue color indicates areas of very low pressure at the center of both stenoses, around 11432 Pa. The pressure gradient in both images reflects a higher complexity, with extremely low pressures at the points of narrowing.

The simulation results in Figure 20 show the pressure distribution of fluid flow with varying stenosis positions in the Bell-Elliptical shape stenosis model (60% stenosis) with a narrowing length of $Lo_1 = Lo_3 = 8$. Figure 20b displays the pressure distribution around a stenosed blood vessel with the same position as in other models. It is clearly seen that the pressure fluctuates as the fluid passes through the stenosis area, where the narrowing of the artery significantly affects the flow behavior. Subsequently, within the stenosis region, there is a drop in pressure (represented by blue) to 10295 Pa. Meanwhile, Figure 20a and 20c show that in the stenosis area, located in the middle of the graph at around an axial distance of 10, there is a pressure drop, indicated by the blue color, which shows that the flow slows down in the stenosis region due to the narrowing of the arterial lumen 8813 Pa. Before and after the stenosis area, the pressure intensifies, as shown by the red and yellow colors, with an interval value of 12255 – 13331 Pa. This pressure distribution indicates that stenosis causes a significant pressure drop in the narrowed area, followed by a pressure recovery as the fluid moves past the stenosis. The higher pressure in the area before the stenosis can exert stress on the arterial walls, posing a risk to the structure of the artery, particularly in the stenosed region.

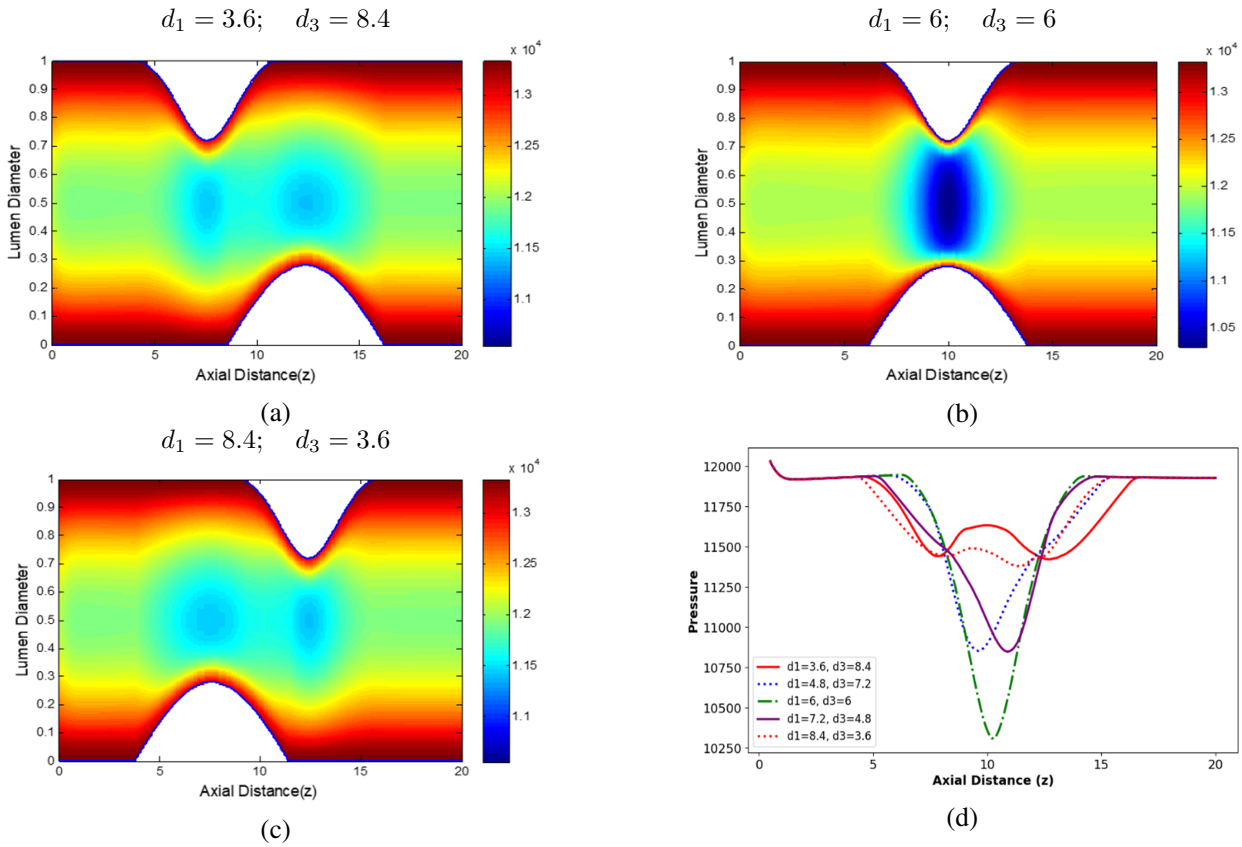

Figure 20. Pressure variation with axial distance for different stenosis positions in Bell-Elliptical shape stenosis.

The next simulation depicts the effect of stenosis length on the flow rate for each developed geometric shape. Based on the simulation results in Figure 21, it is clear that the three graphs collectively show the pressure distribution along the axial distance for various parameter combinations, all indicating a significant pressure drop around the stenosis region. The pressure gradually recovers, with higher values of Lo_1, Lo_2, and Lo_3 resulting in a smaller pressure drop and a smoother transition. The trend is consistent across all graphs, showing that increasing stenosis length can reduce flow resistance, leading to a more stable pressure profile.

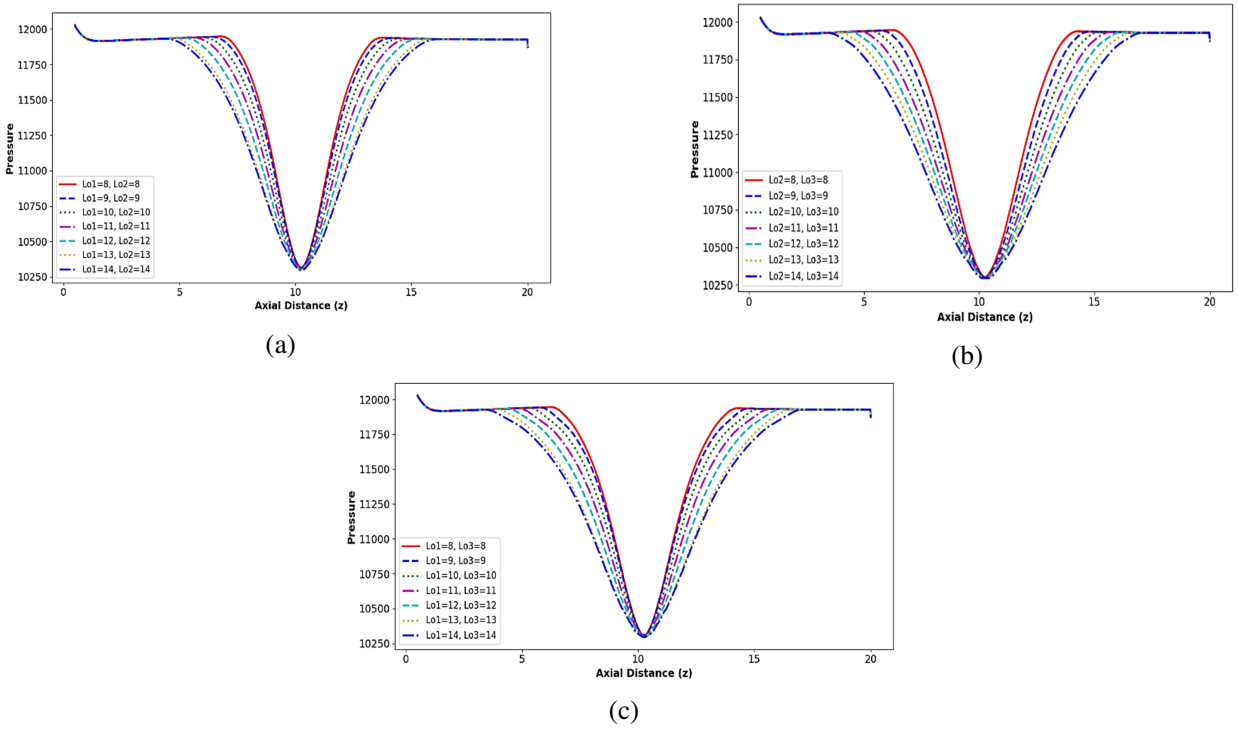

Figure 21. Variation of pressure with axial distance for different stenosis lengths in three asymmetric geometric configurations (a) Bell-Cosine shape (b) Cosine-Elliptical shape (c) Bell-Elliptical shape.

However, this pattern exhibits different variations for each asymmetric stenosis configuration and stenosis length. In Figure 21a, all variations in stenosis length parameters show a significant pressure drop in the middle of the flow before initial pressure recovers. The pressure drop for $Lo_1 = Lo_2 = 8$ (solid red line) is slightly slower compared to the longer stenosis lengths, suggesting that the shape of the stenosis affects the rate of pressure drop and recovery. Figure 21b shows a deeper pressure drop at the stenosis point. Variations in stenosis length parameters reveal smoother pressure changes compared to the Bell-Cosine shape. This indicates that the Cosine-Elliptical geometry produces a sharper pressure drop at the stenosis, but with a quicker recovery after passing the stenosis. The Bell-Elliptical geometry demonstrates characteristics similar to the Bell-Cosine and Cosine-Elliptical shapes but the former has a more moderate pressure drop in the middle of the flow. The pressure decreases more smoothly at $Lo_1 = Lo_3 = 8$, while higher Lo values result in a sharper pressure drop. The comparison of these three shapes shows that the variation in stenosis geometry affects the pressure distribution pattern along the flow. Bell-Cosine produces a more gradual pressure drop, while Cosine-Elliptical tends to cause a sharper drop. Bell-Elliptical falls between the two in terms of moderating the pressure drop.

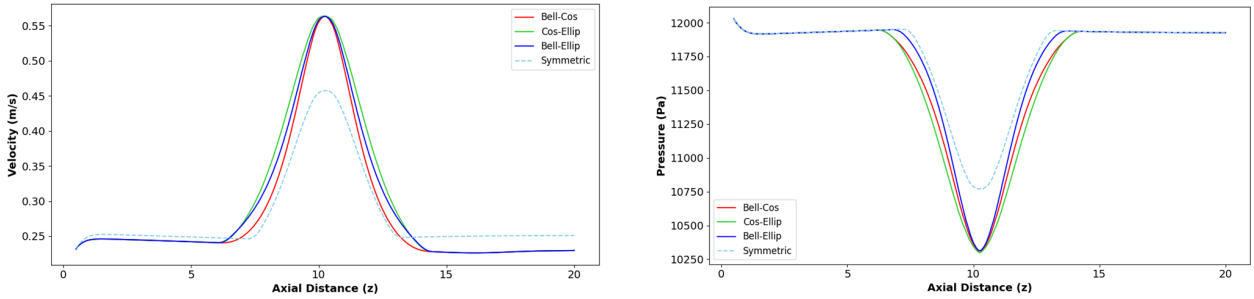

(a) (b)

Figure 22. Variation of blood flow profiles in an artery with stenosis of symmetric, Bell-Cosine, Cosine-Elliptical, and Bell-Elliptical shapes for the following parameters: (a) Flow velocity (b) Pressure distribution.

Asymmetric stenosis shapes exhibit different characteristics compared to symmetric stenosis in terms of fluid velocity distribution and pressure variation. Bell-Cosine produces a gradually increasing velocity profile with a higher peak, indicating a smooth flow transition while still generating significant acceleration. Cosine-Elliptical shares similar characteristics with Bell-Cosine but has a slightly different velocity distribution, resulting in a steeper flow transition. Bell-Elliptical has a sharper slope on its descending side, suggesting more intense fluid acceleration around the stenosis peak. In contrast, the symmetric stenosis results in a lower peak velocity and a more evenly distributed flow, implying that it induces less acceleration compared to asymmetric shapes. Additionally, the relationship between fluid pressure and axial distance reveals a significant pressure drop around the stenosis region. The asymmetric stenosis cases reach nearly the same minimum pressure, while the symmetric profile shows a more gradual pressure decrease. This suggests that asymmetric stenosis causes a sharper pressure drop compared to symmetric stenosis, which distributes pressure more evenly. Overall, asymmetric stenosis tends to enhance fluid acceleration, produce higher peak velocities, and cause more pronounced localized pressure drops, which can influence fluid flow dynamics by increasing acceleration and turbulence effects.

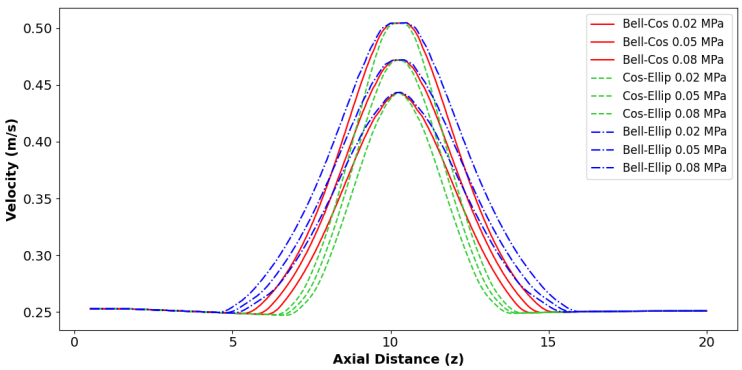

Figure 23. Blood Flow Velocity Distribution for Different Young's Modulus Values in Stenosed Arteries.

Figure 23 illustrates blood flow velocity along the axial distance (z) for different stenosis models (Bell-Cosine, Cosine-Elliptical, and Bell-Elliptical) and varying Young's modulus (E = 0.02, 0.05, 0.08). The Bell-Cosine model exhibits a gradual rise and fall in velocity, reducing shear stress fluctuations but still limiting oxygen supply. The Cosine-Elliptical model demonstrates smoother pressure recovery, which helps minimize turbulence but significantly restricts blood flow. The Cosine-Elliptical model has the sharpest constriction and highest velocity gradient, increasing shear stress and making it the most critical case for Central Retinal Artery Occlusion (CRAO).

The graph also indicates that a higher Young's modulus (stiffer arteries) decreases peak velocity, suggesting greater resistance and reduced perfusion, which can further exacerbate ischemic effects in CRAO.

In general, higher arterial stiffness (higher E) reduces peak blood velocity, as observed in the graph, due to restricted vessel compliance and increased resistance to pulsatile flow. This finding aligns with Roskal et al. in the Journal of Clinical Medicine [37], which highlighted that arterial stiffness can be modulated through specific interventions, suggesting potential therapeutic approaches for Central Retinal Artery Occlusion (CRAO) management. However, the pathological consequences of CRAO due to severe stenosis include retinal ischemia, loss of visual function, and potential permanent blindness if circulation is not restored promptly. These findings underscore the importance of early detection and intervention, where modifying arterial stiffness and optimizing hemodynamics could help mitigate the risk of irreversible retinal damage.

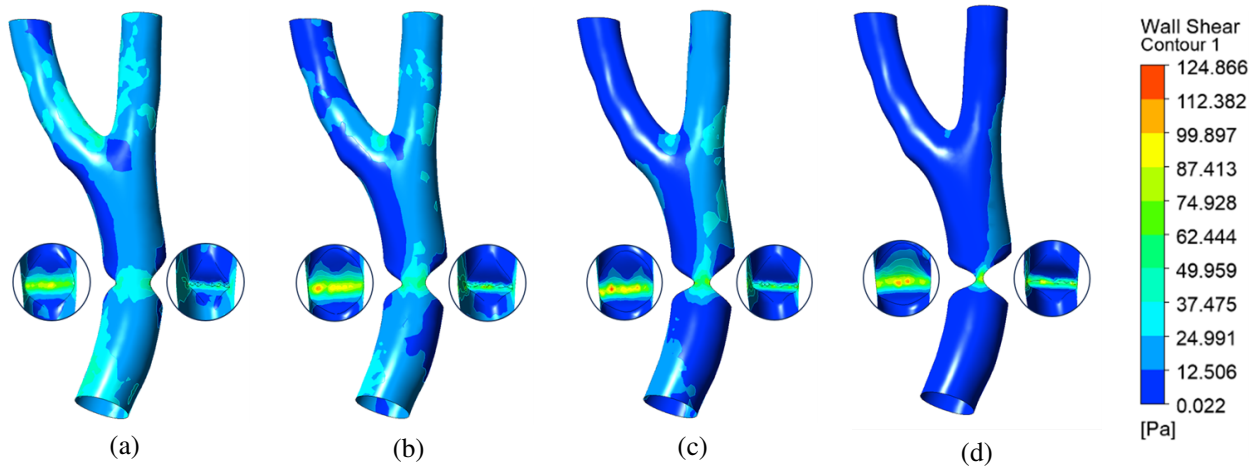

Figure 24. Plot of wall shear on the retinal blood vessel surface of the Bell-Cosine shape model (a) 45% stenosed (b) 60% stenosed (c) 75% stenosed (d) 90% stenosed.

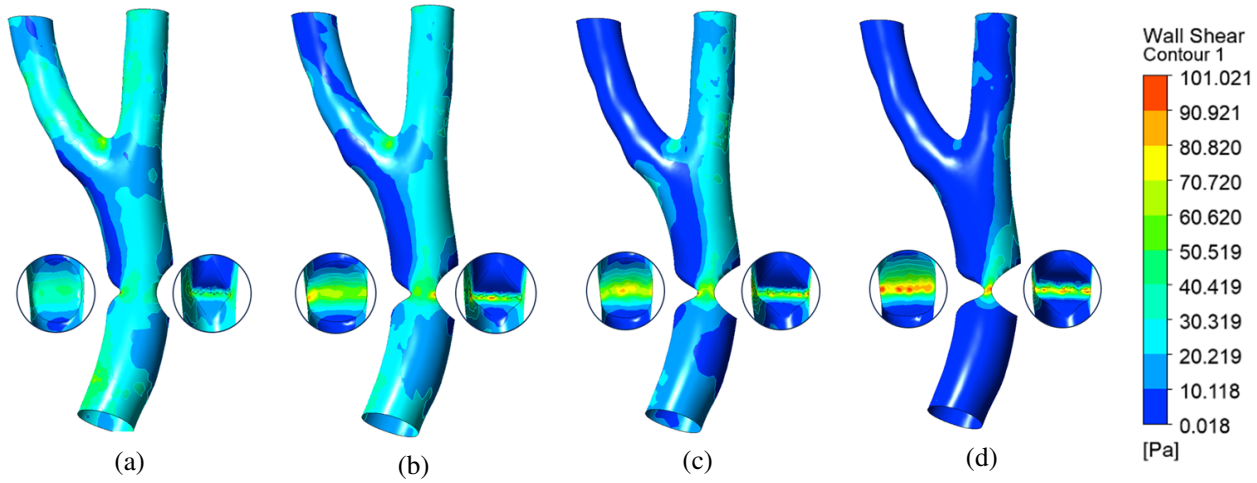

Figure 25. Plot of wall shear on the retinal blood vessel surface of the Bell-Elliptical shape model (a) 45% stenosed (b) 60% stenosed (c) 75% stenosed (d) 90% stenosed.

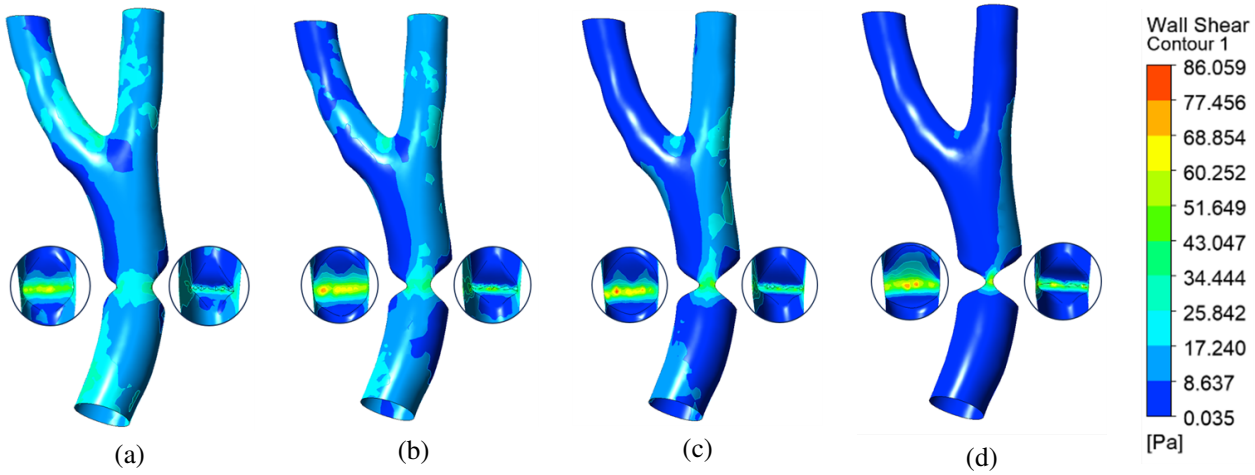

Figure 26. Plot of wall shear on the retinal blood vessel surface of the Cosine-Elliptical shape model: (a) 45% stenosed, (b) 60% stenosed, (c) 75% stenosed, and (d) 90% stenosed.

Based on Figure 24 the Bell-Cosine shape model exhibits the highest wall shear stress (WSS) among the three geometries, particularly at 90% stenosis, where shear stress reaches 124.9 Pa. At 45% – 75% stenosis, WSS remains within a moderate range (25.6 to 75.9 Pa), but the sharp increase at 90% stenosis indicates a critical risk of endothelial damage. This excessive shear force can lead to platelet activation, localized thrombogenesis, and eventual vessel occlusion, making it the most vulnerable model for CRAO development. Additionally, the rapid transition from moderate to extreme WSS values suggests that patients with stenosis patterns resembling the Bell-Cosine model may experience sudden hemodynamic deterioration, requiring early intervention to prevent complete arterial blockage.

The Bell-Elliptical shape model in Figure 25 follows a similar pattern, with WSS increasing as stenosis progresses. At 45%-75% stenosis, the WSS values remain comparable to those in the Bell-Cosine model (25.6 to 75.9 Pa), but at 90% stenosis, the maximum WSS reaches slightly lower values compared to the Bell-Cosine model. While this still presents a risk for endothelial dysfunction and thrombus formation, the gradual increase in WSS suggests a less abrupt transition to critical hemodynamic conditions, potentially allowing more time for therapeutic intervention before complete occlusion occurs. However, since high WSS levels are still present at severe stenosis, this model remains a significant risk factor for CRAO, particularly in cases where compensatory mechanisms fail to maintain adequate retinal perfusion.

The simulation results for the Cosine-Elliptical shape model in Figure 26 show the lowest WSS values among the three geometries, even at 90% stenosis, where peak shear stress remains below those observed in the Bell-Cosine and Bell-Elliptical models. While WSS still increases with stenosis severity, the lower maximum values suggest that this model may be less prone to immediate thrombosis and endothelial damage. However, the presence of regions of low WSS distal to the stenosis raises concerns about atherosclerotic plaque formation and embolization, which could still contribute to retinal artery occlusion over time. Patients with this geometry may have a lower risk of acute CRAO but could still develop chronic vascular instability and progressive ischemia if left untreated.

The three models demonstrate that increased stenosis severity leads to higher WSS, with the Bell-Cosine shape posing the highest risk for CRAO due to extreme shear stress, which may trigger embolus release through endothelial dysfunction, thrombus formation, and microvascular embolization. Clinically, this increase in WSS can serve as an indicator of higher embolus release risk, highlighting the importance of using vascular imaging, such as Doppler ultrasound or OCT angiography, to detect potential central retinal artery occlusion (CRAO) earlier. Patients with Bell-Cosine or Bell-Elliptical stenosis may require more aggressive intervention, such as thrombolytic therapy or endovascular procedures guided by imaging, to prevent total occlusion. Meanwhile, patients with

Cosine-Elliptical stenosis, who have a lower risk, may benefit from long-term vascular monitoring and lipid-lowering therapy to prevent the progression of atherosclerosis. This approach can aid in personalizing treatment and improving clinical outcomes for patients with retinal artery stenosis.

This research has several limitations. First, the fluid is assumed to be Newtonian, with constant viscosity independent of shear stress. This assumption does not account for the characteristics of non-Newtonian fluids, which are more common in real-world applications. Second, the constriction geometry is considered idealized, specifically in the form of bell, cosine, and elliptical shapes. While this simplifies the analysis, it may not accurately reflect the more complex geometries found in real systems. Future research could propose MRI-based models tailored to individual patients, incorporating patient-specific data such as vascular structure, blood flow, and tissue characteristics. Additionally, future studies should explore non-Newtonian fluid models, such as Carreau or Casson, to more accurately represent blood flow characteristics in CRAO and better understand the hemodynamic complexities of this condition. Validating the model in a clinical setting is crucial, involving actual patient data and comparing the results with medical imaging and clinical outcomes. Furthermore, integrating machine learning techniques could enhance the model's predictive capabilities, enabling more precise simulations and personalized treatment plans.

4. Conclusion

A numerical study has been performed to investigate CRAO by scrutinizing three different asymmetric stenotic shapes. A Newtonian fluid flow model and elastic walls were employed to simulate the flow within this arterial segment. The blood flow model through the occluded artery has been validated and simulated under varying occlusion levels, stenosis lengths, and initial stenosis position differences. The present study has drawn the following key findings:

- The velocity profile exhibits higher values near the origin of the stenotic artery region for all asymmetric stenosis geometries.
- The simulation results clearly show that turbulent flow occurs near the stenotic region for all asymmetric stenosis geometries.
- Based on thickness differences, geometries with 90% occlusion show developed laminar flow characteristics, which could lead to the rupture of atherosclerotic plaques in the stenosis, potentially causing blood clots or thrombosis.
- Pressure peaks are observed near the sharp corners of the stenotic segment.
- The Cosine-Elliptical shape model yields the highest flow velocity compared to the other two models, while the Bell-Cosine shape model generates higher pressure and wall shear stress around the stenosis area than the other two models.
- The stenosis length does not significantly affect the flow velocity; it only increases the laminar flow area in the center of the stenosis region.
- The authors plan to further develop this research using actual stenosis geometries on patient-specific geometries extracted from MRI scans.

Acknowledgments

The present research was fully supported by the laboratory of modelling and simulation (Limosim), Department of Mathematics, Sepuluh Nopember Institute of Technology, Surabaya, Indonesia.

REFERENCES

1. S. Gupta, M. Aryal, Y. Rajbhandari, A. Adhikari, V. Kamble, and B. Aryal, "Central Retinal Artery Occlusion Associated with Atrial Septal Defect: A Case Report," *J Lumbini Med Coll*, vol. 7, pp. 34-36, 2019. doi: https://doi.org/10.22502/jlmc.v7i1.281.
2. C. Hoyer, C. Kahlert, R. Güney, F. Schlichtenbrede, M. Plattén, and K. Szabo, "Central retinal artery occlusion as a neuro-ophthalmological emergency: the need to raise public awareness," *European Journal of Neurology*, vol. 28, 2021. doi: https://doi.org/10.1111/ene.14735.
3. B. Grory, M. Schrag, V. Biousse, K. Furie, M. Gerhard-Herman, P. Lavin, L. Sobrin, S. Tjoumakaris, C. Weyand, and S. Yaghi, "Management of Central Retinal Artery Occlusion: A Scientific Statement From the American Heart Association," *Stroke*, vol. 52, pp. e282-e294, 2021. doi: https://doi.org/10.1161/STR.0000000000000366.
4. S. S. Hayreh, "Acute retinal arterial occlusive disorders," *Progress in Retinal and Eye Research*, vol. 30, pp. 359-394, 2011. doi: https://doi.org/10.1016/j.preteyeres.2011.05.001.
5. M. Schumacher, D. Schmidt, B. Jurklies, C. Gall, I. Wanke, C. Schmoor, H. Maier-Lenz, L. Solymosi, H. Brueckmann, A. Neubauer, A. Wolf, and N. Feltgen, "Central retinal artery occlusion: local intra-arterial fibrinolysis versus conservative treatment, a multicenter randomized trial," *Ophthalmology*, vol. 117, pp. 1367-1375, 2010. doi: https://doi.org/10.1016/j.ophtha.2010.03.061.
6. D. D. Varma, S. Cugati, A. W. Lee, and C. S. Chen, "A review of central retinal artery occlusion: clinical presentation and management," *Eye (Lond)*, vol. 27, pp. 688-697, 2013. doi: https://doi.org/10.1038/eye.2013.25.
7. E. Prewitt, "Clinical Findings and Management of Central Retinal Artery Occlusion," *CRO (Clinical & Refractive Optometry) Journal*, vol. 32, pp. 342-346, 2021. doi: https://doi.org/10.57204/001c.36884.
8. Menaouer, Brahami & Dermane, Zoulikha & Kebir, Nour & Nada, Matta, "Diabetic Retinopathy Classification Using Hybrid Deep Learning Approach" *SN Computer Science*, vol. 3, pp. 1-15, 2021. doi: https://doi.org/10.1007/s42979-022-01240-8.
9. J. Malek, A. T. Azar, B. Nasralli, M. Tekari, H. Kamoun, and R. Tourki, "Computational analysis of blood flow in the retinal arteries and veins using fundus image," *Computers & Mathematics with Applications*, vol. 69, pp. 101-116, 2015. doi: https://doi.org/10.1016/j.camwa.2014.11.017.
10. A. Dagra, B. Lucke-Wold, K. McGrath, I. Mehkri, Y. Mehkri, C. Davidson, N. Gilberstadt, B. Douglas, and B. Hoh, "Central Retinal Artery Occlusion: A Review of Pathophysiological Features and Management," *Stroke: Vascular and Interventional Neurology*, vol. 4, pp. e000977, 2023. doi: https://doi.org/10.1161/svin.123.000977.
11. D. N. Ku, "Blood Flow In Arteries," *Annual Review of Fluid Mechanics*, vol. 29, pp. 399–434, 1997. doi: https://doi.org/10.1146/annurev.fluid.29.1.399.
12. J. Nadal, A. Wu, and M. Canut, "Vitrectomy With Intrasurgical Control of Ocular Hypotony as a Treatment for Central Retina Artery Occlusion," *Retina*, vol. 35, pp. 1704-1705, 2015. doi: https://doi.org/10.1097/IAE.0000000000000702.
13. Z. Lu, X. Wu, F. Cai, F. Huang, S. Liu, and Y. Yang, "Error estimates in L^2 and L^∞ norms of finite volume method for the bilinear elliptic optimal control problem," *AIMS Mathematics*, vol. 6, pp. 8585-8599, 2021. doi: https://doi.org/10.3934/math.2021498.
14. M. K. Jain and P. D. Wolf, "A Three-Dimensional Finite Element Model of Radiofrequency Ablation with Blood Flow and its Experimental Validation," *Annals of Biomedical Engineering*, vol. 28, pp. 1075–1084, 2000. doi: https://doi.org/10.1114/1.1310219.
15. R. Madike, S. Cugati, and C. Chen, "A review of the management of central retinal artery occlusion," *Taiwan Journal of Ophthalmology*, vol. 12, pp. 273 - 281, 2022. doi: https://doi.org/10.4103/2211-5056.353126.
16. P. Owasit and S. Sriyab, "Mathematical modeling of non-Newtonian fluid in arterial blood flow through various stenoses," *Adv Differ Equ*, vol. 340, pp. 1-20, 2021. doi: https://doi.org/10.1186/s13662-021-03492-9.
17. A. Mwapinga, E. Mureithi, M. N. James, and V. Masanja, "MHD Arterial Blood Flow and Mass Transfer under the Presence of Stenosis, Body Acceleration and Chemical Reaction: A Case of Magnetic Therapy," *Journal of Mathematics and Informatics*, vol. 18, pp. 85-103, 2020. doi: https://doi.org/10.22457/jmi.v18a8164.
18. R. Ellahi, S. U. Rahman, S. Nadeem, and N. S. Akbar, "Blood flow of nanofluid through an artery with composite stenosis and permeable walls," *Applied Nanosci*, vol. 4, pp. 919–926, 2014. doi: https://doi.org/10.1007/s13204-013-0253-6.
19. A. Hussain, M. N. R. Dar, W. K. Cheema, E. M. Tageldin, and R. Kanwal, "Numerical simulation of unsteady generic Newtonian blood flow and heat transfer through discrepant shaped dilatable arterial stenosis," *Results in Engineering*, vol. 18, pp. 101189, 2023. doi: https://doi.org/10.1016/j.rineng.2023.101189.
20. B. Tripathi and B. Sharma, "Two-phase analysis of blood flow through a stenosed artery with the effects of chemical reaction and radiation," *Ricerche di Matematica*, vol. 73, pp. 151–177, 2024. doi: https://doi.org/10.1007/s11587-021-00571-7.
21. R. Ponalagusamy and R. Manchi, "A study on two-layered (K.L-Newtonian) model of blood flow in an artery with six types of mild stenoses," *Applied Mathematics and Computation*, vol. 367, pp. 124767, 2019. doi: https://doi.org/10.1016/j.amc.2019.124767.
22. S. Kumar and S. Kumar, "Blood Flow with Heat Transfer through Different Geometries of Stenotic Arteries," *Trends in Sciences*, vol. 20, pp. 1-14, 2023. doi: https://doi.org/10.48048/tis.2023.6965.
23. E. K. Ata and I. Kandemir, "Examination of non-Newtonian flow through stenosed arteries using an analytical model," *Archive of Applied Mechanics*, vol. 92, pp. 3179-3202, 2022. doi: https://doi.org/10.1007/s00419-022-02230-1.
24. J. Malek and A. Azar, "A computational flow model of oxygen transport in the retinal network," *Int. J. Model. Identif. Control*, vol. 26, pp. 361-371, 2016. doi: https://doi.org/10.1504/IJMIC.2016.081138.
25. H. Afrasiab, "A fluid-structure interaction study vulnerability different coronary plaques to blood flow increase during physics exercise," *AUT J. Mech. Eng*, vol. 2, pp. 51-60, 2018. doi: https://doi.org/10.22060/mej.2017.13415.5625.
26. S. R. H. Barret, M. P. F. Sutcliffe, S. Howarth, Z. Y. Li, and J. H. Gillard, "Experimental measurement of the mechanical properties of carotid atherothrombotic plaque fibrous cap," *J. Biomech*, vol. 42, pp. 1650-1655, 2009. doi: https://doi.org/10.1016/

j.jbiomech.2009.04.025.
27. S. A. Kock, J. V. Nygaard, N. Eldrup, E. T. Frund, A. Klaerke, W. P. Paaske, E. Falk, and W. Yong Kim, "Mechanical stresses in carotid plaques using MRI-based fluid-structure interaction models," *J. Biomech*, vol. 41, pp. 1651-1658, 2008. doi: https://doi.org/10.1016/j.jbiomech.2008.03.019.
28. H. G. Matthies and J. Steindorf, "Partitioned strong coupling algorithms for fluid-structure interaction," *Comput. Struct.*, vol. 81, pp. 805-812, 2003. doi: https://doi.org/10.1016/S0045-7949(02)00409-1.
29. S. Pabi, M. K. Khan, S. K. Jain, A. K. Sen, and A. Raj, "Effect of stenotic shapes and arterial wall elasticity on the hemodynamics," *Physics of Fluids*, vol. 35, pp. 1-27, 2023. doi: https://doi.org/10.1063/5.0169575.
30. D. Goldenberg, J. Shahar, A. Loewenstein, and M. Goldstein, "Diameters of retinal blood vessels in a healthy cohort as measured by spectral domain optical coherence tomography," *Retina*, vol. 33, pp. 1888–1894, 2013. doi: https://doi.org/10.1097/iae.0b013e31829477f2.
31. M. Roy, B. S. Sikarwar, M. Bhandwal, and P. Ranjan, "Modelling of blood flow in stenosed arteries," *Procedia Computer Science*, vol. 115, pp. 821-830, 2017. doi: https://doi.org/10.1016/j.procs.2017.09.164.
32. A. W. Vaes, M. A. Spruit, N. Goswami, J. Theunis, F. M. E Franssen, and P. D. Boever, "Analysis of Retinal Blood Vessel Diameters in Patients With COPD Undergoing A Pulmonary Rehabilitation Program," *Microvascular Research*, vol. 139, 2022. doi: https://doi.org/10.1016/j.mvr.2021.104238.
33. Yuhong Zhao, Jue Xie, "Numerical analysis of blood flow through stenosed microvessels using a multi-phase model," *Heliyon*, vol. 10, 2024. doi: https://doi.org/10.1016/j.heliyon.2024.e29843.
34. D.B. Camasão, D. Mantovani, "The mechanical characterization of blood vessels and their substitutes in the continuous quest for physiological-relevant performances" *A critical review, Materials Today Bio*, vol. 10, 2021. doi: https://doi.org/10.1016/j.mtbio.2021.100106.
35. H. K. Versteeg and W. Malalasekera, *An Introduction to Computational Fluid Dynamics – The Finite Volume Method*, Prentice-Hall Inc, 2007, Edinburgh Gate, England.
36. J. H. Ferziger and M. Perić, *Computational Methods for Fluid Dynamics*, Springer, 2002.
37. Roskal-Wałek, J., Wałek, P., Biskup, M., Sidło, J., Cieśla, E., Odrobina, D., Mackiewicz, J., & Wożakowska-Kapłon, B, "Retinal Artery Occlusion and Its Impact on the Incidence of Stroke, Myocardial Infarction, and All-Cause Mortality during 12-Year Follow-Up" *Journal of Clinical Medicine*, vol. 11, 2022. doi: https://doi.org/10.3390/jcm11144076.